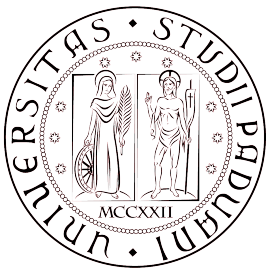

Università degli Studi di Padova

Dipartimento di Ingegneria Industriale

Master Degree in Aerospace Engineering

Development of a multiaxial force sensor for docking systems characterization

Author:

Matteo Veronese
2048419

Supervisor:

Prof. Francesco Branz

Academic Year 2022/2023

Abstract

This thesis presents the development of a multi-axial force sensor (MAFS) designed specifically for docking systems. Docking between two satellites occurs when the probe of the chaser satellite connects with the drogue of the target satellite. In order to better understand this dynamic process, it is crucial to measure the forces exchanged between the probe and drogue during impact. The MAFS developed in this research is capable of measuring dynamic loads in two directions and at an appropriate sampling rate, providing valuable insights on the impact dynamics.

The construction of the MAFS involves the use of 3D printed joints, milled plates, and four load cells. Two load cells are responsible for measuring frontal loads, while the remaining two measure lateral loads. The output signals from the load cells are amplified and acquired through an analog-to-digital converter.

To establish the relationship between force and voltage, each load cell undergoes individual calibration using known weights, employing a linear model.

Static tests are carried out in the frontal and lateral directions to verify the accuracy of the MAFS.

The dynamic behavior of the MAFS is validated through a series of drop tests utilizing a pulley and drop weight setup, confirming the impulse momentum equivalence. For the dynamic tests, a high precision and high frequency motion capture system provides the positional data.

Eventually, to test docking loads, the MAFS is mounted to the edge of a low-friction table, which replicates the low gravity conditions of satellite docking. Acting as the target, the MAFS interacts with a small satellite with gas cushions that floats on the table, serving as the chaser. The probe mounted on the MAFS collides with the drogue on the chaser, and the resulting loads are measured.

Riassunto esteso

Questa tesi presenta lo sviluppo di un sensore di forza multiassiale (MAFS) progettato specificamente per i sistemi di docking. Il docking tra due satelliti avviene quando la probe del chaser si collega alla drogue del target. Per comprendere meglio questa dinamica, è cruciale misurare le forze scambiate tra probe e drogue durante il docking. Il MAFS, sviluppato durante questa ricerca, misura carichi dinamici in due direzioni e con un'adeguata frequenza di campionamento, fornendo informazioni preziose sui carichi di docking.

La costruzione del MAFS prevede l'uso di giunti stampati in 3D, piastre fresate e quattro celle di carico. Due celle di carico sono responsabili della misura dei carichi frontali, mentre le altre due misurano i carichi laterali. I segnali in uscita dalle celle di carico vengono amplificati e acquisiti tramite un convertitore analogico-digitale.

Per stabilire la relazione tra forza e tensione, ogni cella di carico viene calibrata utilizzando pesi noti, utilizzando un modello lineare.

Vengono poi effettuati test statici nelle direzioni frontale e laterale per verificare l'accuratezza del MAFS.

Il comportamento dinamico del MAFS viene convalidato attraverso una serie di test di caduta che utilizzano una configurazione a carrucola e peso cadente, confermando l'equivalenza impulso-momento. Per i test dinamici, un sistema di motion capture ad alta precisione ed alta frequenza fornisce i dati di posizione necessari.

Infine, per testare i carichi di docking, il MAFS rappresenta il target e viene montato sul bordo di un tavolo a basso attrito che replica le condizioni di gravità ridotta tipiche del docking. Il chaser consiste in un piccolo satellite dotato di cuscinetti ad aria che fluttua sul tavolo. La probe montata sul MAFS collide con la drogue montata sul satellite chaser, misurando i carichi risultanti.

Contents

Introduction

In recent years new solutions for commercial orbital systems are emerging. Some of these systems involve fleets or constellations of small satellites that operate as a whole to achieve better performances in telecommunication and Earth observation activities. Among other capabilities, On-Orbit Servicing and On-Orbit Assembly might be needed to maintain and upgrade the fleets of small satellites. These operations are usually performed once a rigid connection, provided by the docking mechanism, is established between the satellite and another orbiting vehicle [1].

One of the most simple and common docking configurations for small satellites is the probe-drogue. Fig. 1 provides an example of probe-drogue with a self-centering design and a latching mechanism.

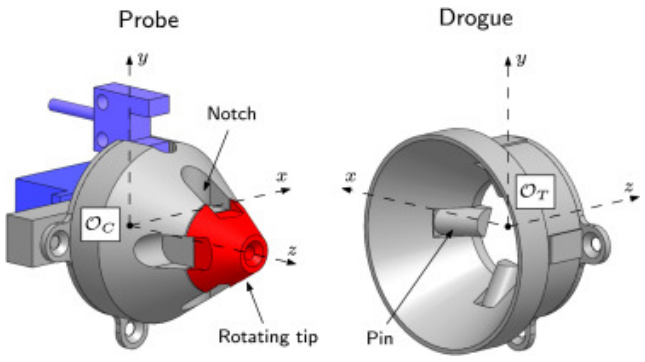

Figure 1: Example of drogue-probe docking mechanism [1]

1.1 Measuring docking loads

Designing a reliable docking mechanism requires accurate knowledge of the dynamics of the impact originated from the contact between the two parts of the docking mechanism. Since the impact happens in a low gravity environment, the testing setup has to be designed accordingly.

One method to characterize this kind of impact consists of measuring the loads exchanged during the contact between the two bodies. This can be done with a force sensor.

The orbital environment has to be replicated in the laboratory. The chosen approach is to utilize a low-friction table. The force sensor can be mounted at the edge of the low-friction table, onto which a satellite mockup is free to move. The satellite mockup has to resemble the actual one in inertia and dimensions, and is fitted with gas bearings. The low-friction table consists in a flat and levelled surface, onto which the gas bearings hover. The impact happens when the satellite is pushed towards the sensor and the probe (mounted on the satellite) hits the drogue (mounted on the force sensor). Additionally, the positional data of the satellite can be acquired with a motion capture setup.

1.2 Developing a custom multi-axis sensor

In order to evaluate the impact dynamics and the docking performances, a force sensor that measures along a single axis is not sufficient. Even if the majority of the impact load is frontal, being able to measure the lateral loads allows to better understand the dynamics and how the probe-drogue mechanism is solicited.

Whilst commercially available multi-axis force sensors exist, they have some shortcomings. They are usually developed with specific applications in mind, which make them difficult to be integrated in different use cases and often very expensive. Moreover, they are offered in limited load capacities. It is also worth noting that even commercially available solutions would need extensive calibration tests because multi-axis sensors are affected by coupling errors determined by the sensor's structure [10]. For these reasons, developing a custom sensor seems the best path to take: the flexibility and reliability offered by a

custom solution outweigh the initial development effort required.

This thesis will illustrate the phases of development of a multi-axis force sensor, in particular:

1. Design and manufacturing (Chapter 2)
2. Static calibration at component level (Chapter 4) and system level (Chapter 5)
3. Dynamic calibration of the sensor (Chapter 6)
4. Integration ad utilization of the sensor in the laboratory facility (Chapter 7)

System design

The sensor, capable of measuring the loads exchanged during a docking along more than one axis, will be called *Multi-axial force sensor* (MAFS). The MAFS is developed from scratch, taking advantage of the facilities of the Università degli Studi di Padova.

2.1 Design principles

The initial design phase is driven by some key design drivers:

- Maximizing stiffness and rigidity
- Minimizing the torque caused by distance of the centre of mass from the load sensor axis
- Favoring simplicity and future developments

The MAFS needs to be rigid enough to withstand the impacts, avoiding fractures and misalignments. The alignment is particularly important when dealing with docking mechanism, because the relative position between the probe and drogue affects the impact dynamics.

The MAFS structure should be designed to maximize the peak response frequency. In particular, the structure should be stiffer than the load cells, assuring that the load cells are the first to bend under load, registering the correct loads.

In order to minimize the torque caused by an off-centred centre of mass, a "compact" sensor is preferred, keeping the lever arm as small as possible.

The simplicity requirement comes from a practical point of view: given the laboratory application of the sensor, being able to test, assemble, and modify the sensor faster is definitely useful. Part of the simplicity criteria also consists in the research of symmetries: symmetric components can be swapped easily and help obtaining a balanced structure.

2.2 Sensing technology choice

The are many technologies available to measure loads. Electrical resistance strain gauges (ERSGs) are a popular and reliable category of sensing technologies. ERSGs exploit the geometry deformation to produce a variation in electrical resistance [10]. Load cells belong to the ERSGs category and come in different geometries and capacities. The capacity of a load cell is the maximum load (or weight) that the cell is able to measure.

The MAFS utilizes four single-point load cells. This type of load cell has a suitable geometry (sample in Fig. 2) and its mounting requirements are compatible with the MAFS design.

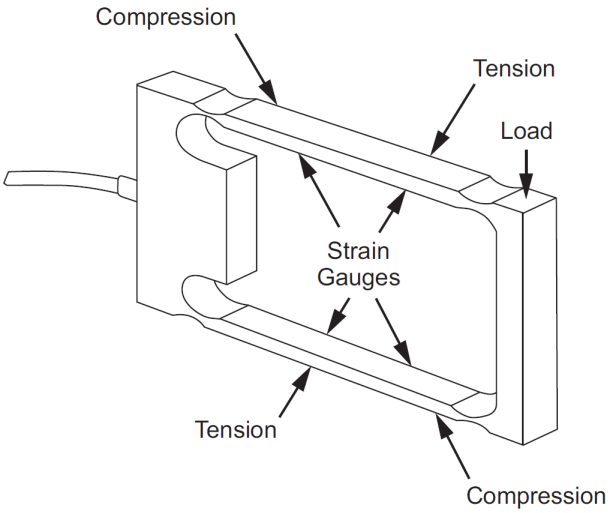

Figure 2: Single point load cell [5]

Ideally, measuring the loads on all three directions is optimal. In reality, the third axis, aligned with gravity, would not be meaningful because it is always affected by gravity itself or other reaction forces. Hence, the MAFS is

going to be bi-axial: it measures the impact loads in the frontal direction and in one lateral direction.

Two load cells are needed for each direction because this gives symmetry and stiffness to the sensor.

The load cells are named as follows. Fig. 3 shows how the load cells are arranged, utilizing the MAFS reference frame.

- *Cell 1*, measuring along the frontal (+x) direction
- *Cell 2*, measuring along the frontal (+x) direction
- *Cell 3*, measuring along the lateral (+y) direction
- *Cell 4*, measuring along the lateral (-y) direction

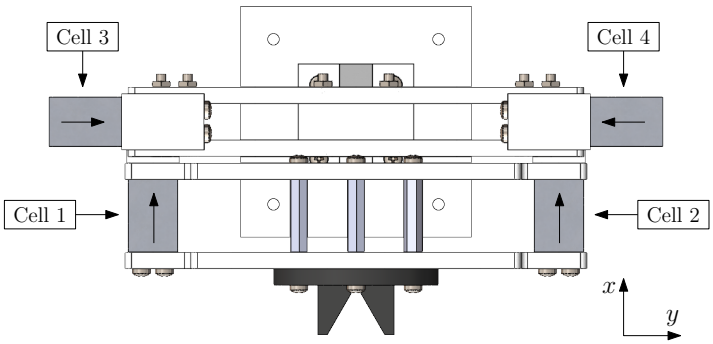

Figure 3: CAD model top view. Arrows indicate the load cell sensing direction

2.3 Final design

The structure of the MAFS is composed by:

- 4x load cells

- 4x 3D printed PLA joints
- 4x milled 5 mm PVC plates
- 16x M3 screws of various lengths
- 8x M3 nuts
- 3x M3 standoffs
- 1x 3D printed PLA stand (optional)

The final design has been reached after some iterations, with many improvements aimed at fulfilling the design principles mentioned in Section 2.1. The most relevant are:

- Instead of simple PVC plates, two sandwich structures are used, with the PLA joints clamped between two plates. This greatly increases the rigidity of the structure.
- Three standoffs are placed between the two frontal plates. This is done to evenly distribute the load between the two plates.
- The joints are 3D printed using high infill density, thick walls and tight tolerances.
- Any connection between two pieces is done with at least two screws in order to completely remove any slack.
- Countersunk screws are used to further reduce the distance between the centre of mass and the load cells axis.

Figures Figure 6, Figure 4 and Figure 5 show the CAD drawings of the final MAFS design. The stand may change depending on where the MAFS is mounted.

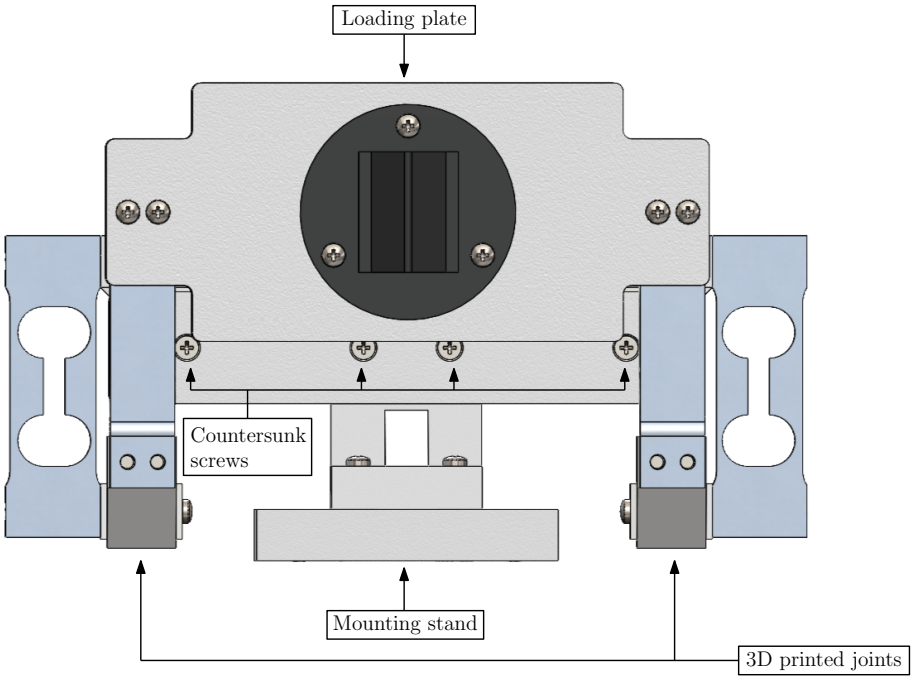

Figure 4: CAD model of the MAFS, frontal view

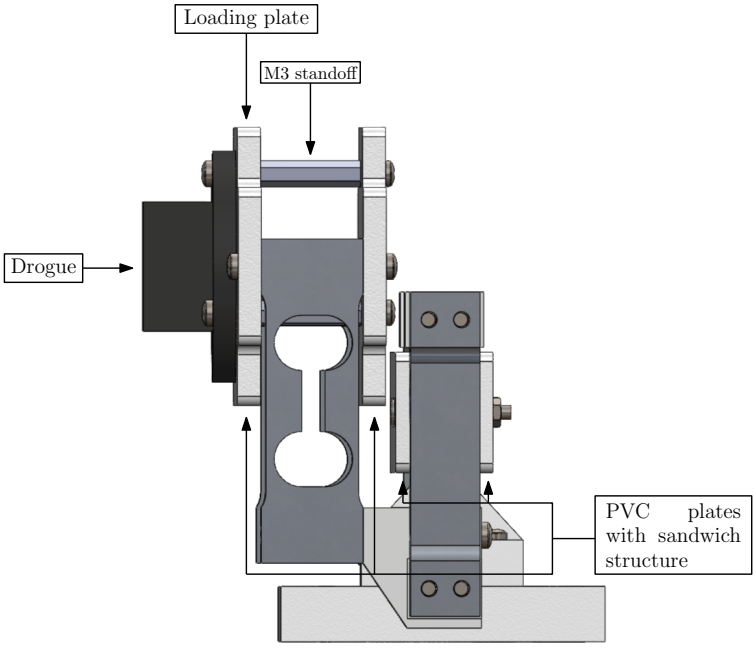

Figure 5: CAD model of the MAFS, lateral view

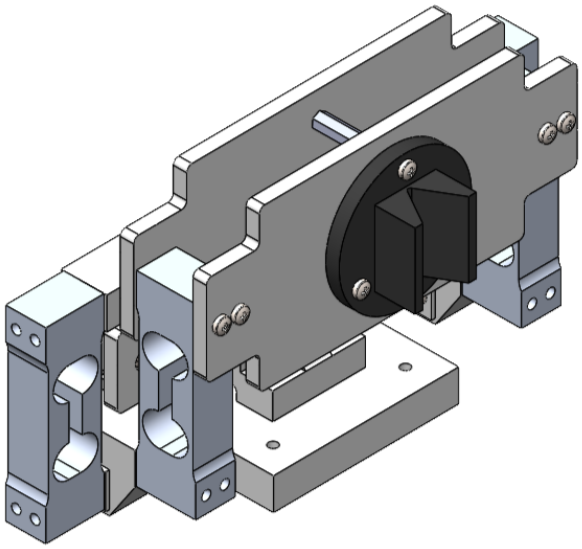

Figure 6: CAD model of the MAFS, perspective view

System configuration

The components used to acquire the MAFS output in MATLAB are schematized in Fig. 7. Each component needs to be correctly wired and configured.

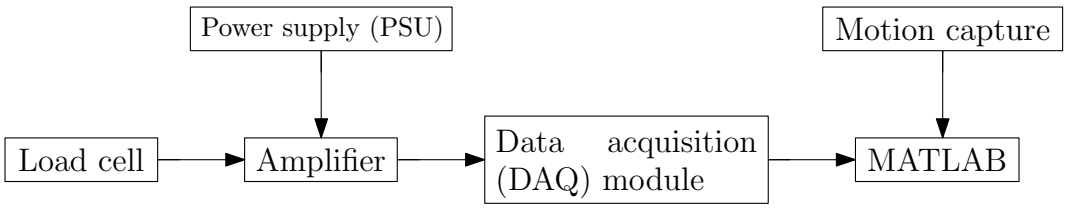

Figure 7: System components diagram

3.1 Load cell

The MAFS utilizes four *Tedea Huntleigh model 1006* load cells (Fig. 8). The two frontal load cells (Cell 1 & 2) have a capacity of 5 kg, whilst the lateral ones (Cell 3 & 4) have a capacity of 2 kg.

They belong to the Electrical resistance strain gauges (ERSGs) category. Each load cell has four wires following the unbalanced Wheatstone bridge configuration [9]. The outputs are listed in Table 1.

Figure 8: Tedea Huntleigh model 1006 Load Cell [9]

Table 1: Outputs for Tedea Huntleigh model 1006 load cell [9]

Color	Output
Green	+VE input
Red	+VE output
Black	−VE input
White	−VE output

3.2 Power supply

The power supply (PSU) used is an *Aim-TTi EX752M*, pictured in Fig. 9. It is a 300 W power supply, with dual 0 to > 75 V and 0 to > 2 A outputs. The 3-digit display provides a resolution of 100 mV with an accuracy of 0.3% of the reading ± 1 digit [2].

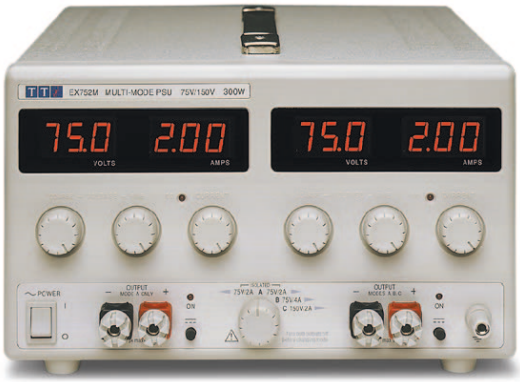

Figure 9: Aim-TTi EX752M [2]

Only one of the two PSU outputs is used by the MAFS, with the output voltage set at 10.0 V and the current limiter not engaged.

3.3 Amplifier

The output voltage difference provided by the load cells is in the order of the millivolts. Such small voltages cannot be read by the analog-to-digital converter, hence the need to amplify the signal.

To accomplish this task four *Synectic Design SY011* bridge amplifiers are used. The specific model number is *SY011V100-10-02*, which has ±10 V output, 10 V excitation, and 2 mV/V sensitivity [8].

Two fine adjustment trimmers are used to trim the span and the zero level. Both trimmers have 22 turns and are non-interactive, meaning that adjusting the span does not influence the zero level and vice versa.

The zero level has to be adjusted so that the output of each load cell is about zero when unloaded. This regulation does not need to be precise, as a finer zeroing will be done via software. The only goal at this point is preventing that the load cells output exceeds the amplifier range of ±10 V: if the baseline is too high or too low when unloaded, the load cells could reach the 10 V limit once they are loaded, saturating the amplifier and providing wrong readings.

Figure 10: Synectic Design SY011 [8]

The amplifier needs to be powered at 5 V. Because the PSU outputs 10 V, a voltage divider is used to cut the voltage by half. It is composed of two resistors with the same electrical resistance R. Fig. 11 illustrates the whole wiring schematic.

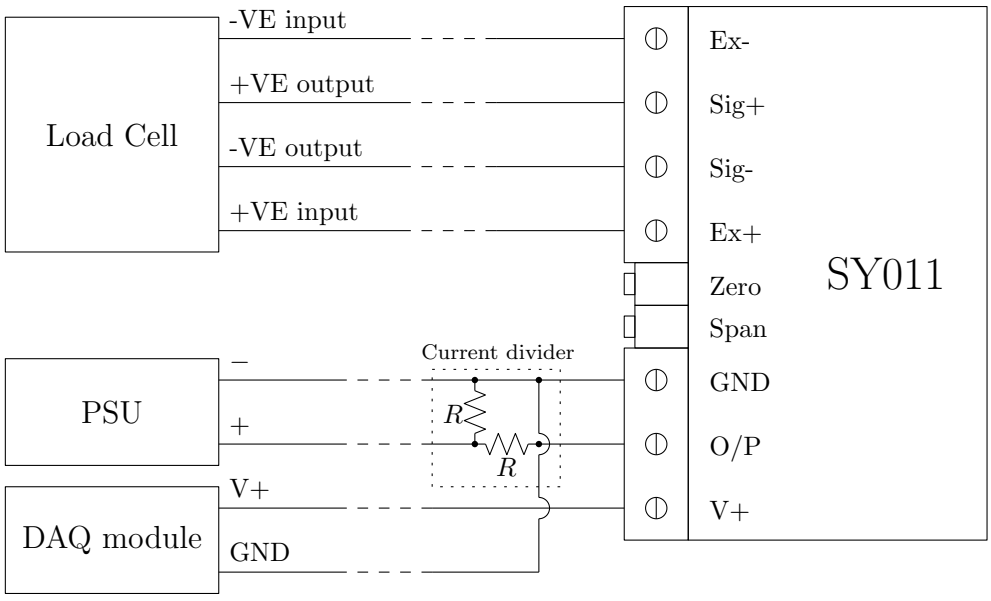

Figure 11: Amplifier schematic

3.4 DAQ module

The data acquisition (DAQ) module used is the *Measurement Computing USB-1408FS-Plus*, pictured in Fig. 12. It is an analog to digital converter with I/O data acquisition functionalities to record and transfer the input data to the PC via USB [11].

1	Screw terminal pins 21 to 40	3	Screw terminal pins 1 to 20
2	LED	4	USB connector

Figure 12: Measurement Computing USB-1408FS-Plus [11]

It supports up to eight single-ended inputs or four differential inputs, depending on the configuration. Two main configurations are available:

1. Differential input mode: the input signal is measured as the difference between the high input and the low input.
   The V+ and GND signals of each load cell amplifier will have to be connected to the reader as shown in Fig. 13.

2. Single-ended input mode: the input signal is referenced to signal ground (GND).
   The V+ signal of each load cell's amplifier will have to be connected to the reader, whilst only one GND signal is used as reference by all the inputs. Fig. 14 shows the wiring diagram.

It is possible to operate the MAFS in single-ended mode because all the amplifiers share the same power source and, ignoring electrical disturbs, the reference voltage (GND) is the same across all four amplifiers.

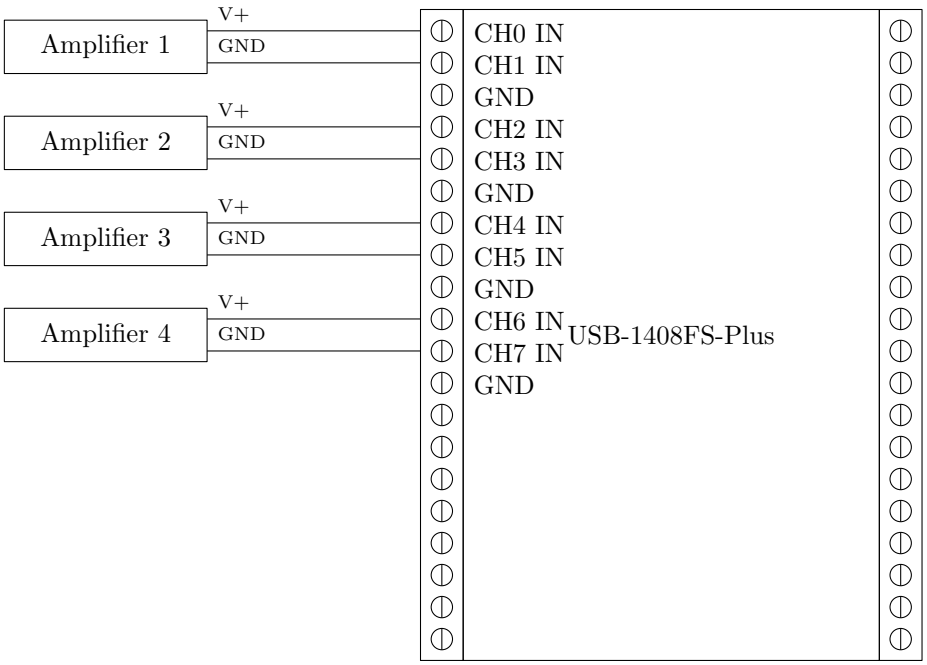

Figure 13: Differential input mode schematic, only relevant pins are indicated

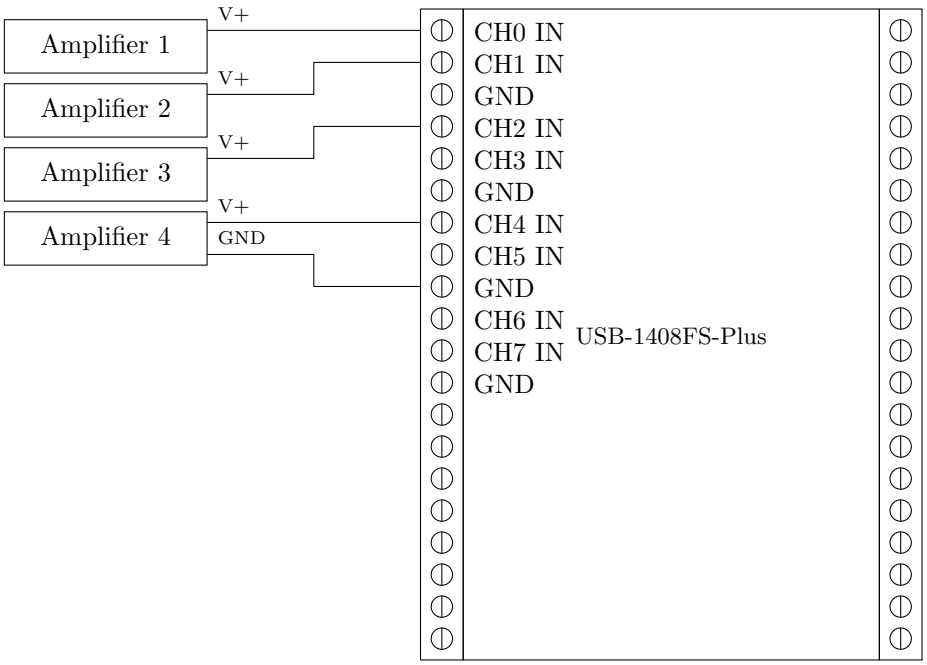

Figure 14: Single-ended input mode schematic, only relevant pins are indicated

The maximum sampling rate depends on the number of channels scanned and the values are in Table 2. Single-ended mode requires one channel per input (GND does not count as an input channel), whilst differential mode requires two channels per input. This means that the maximum sampling rate reached with four differential inputs is 6 kS/s, whilst it can reach 12 kS/s in single-ended mode. Even though the differential mode reduces signal noise, the single-ended mode has been preferred because of the higher sampling rate.

Table 2: Measurement Computing USB-1408FS-Plus sampling rates [11]

# channels scanned	Sample rate (kS/s)
1	48
2	24
3	16
4	12
5	9.60
6	8
7	6.85
8	6

The DAQ module is connected to a PC via USB and the acquired data can be read in MATLAB after the proper drivers are installed. Two add-ons are also required by MATLAB: *Data Acquisition Toolbox* and *Data Acquisition Toolbox Support Package for Measurement Computing Hardware*. The relevant lines of code for the data acquisition script are listed in Appendix A.1.

3.5 Motion capture

The positional data is acquired using a motion capture system installed in the laboratory. The setup is composed of four *Primex 13W* infrared cameras by *Optitrack*.

The setup main specifications are:

- Resolution: 1.3 MP
- 3D accuracy: ±0.3 mm

- Frame rate: 240 FPS
- Latency: 4.2 ms

Reflective markers are mounted on the objects that need to be tracked. In the motion capture software (Motive), any group of three or more markers can be used to define a rigid body. Motive generates a series of frames that contain the instantaneous positional data of the rigid bodies tracked. Motive also acts as a local server. It is necessary to configure the data transmission with the settings shown in Fig. 15; specifically, to set *Transmission type* to *Unicast*, *Broadcast Frame* to *On* and *Rigid Bodies* to *On*. Optitrack offers an SDK to communicate with the Motive server from the MATLAB environment.

In the data acquisition script, some libraries (provided by the NatNet SDK) have to be imported and initialized. Once the communication with the server is established, a MATLAB *listener* is defined. Each time a new frame is ready, the server triggers the listener. A *callback function* is executed asynchronously each time the listener is triggered. That function processes the data contained in the new frame. This approach is preferred to the polling method [3] because it ensures that the data reception is done in a standalone process (the callback function). If an error occurs while receiving or processing a frame, it will not block the main data acquisition script. This also guarantees that all the frames available on the server are received, no matter what their spacing in time is.

Once the event listener is defined, it remains enabled during the acquisition period and is disabled afterwards. The callback function uses vectors to store the positional data and the timestamp contained in frame. The data is then aggregated into a *timetable*. The timetable is a type of MATLAB table that associates a time with each row.

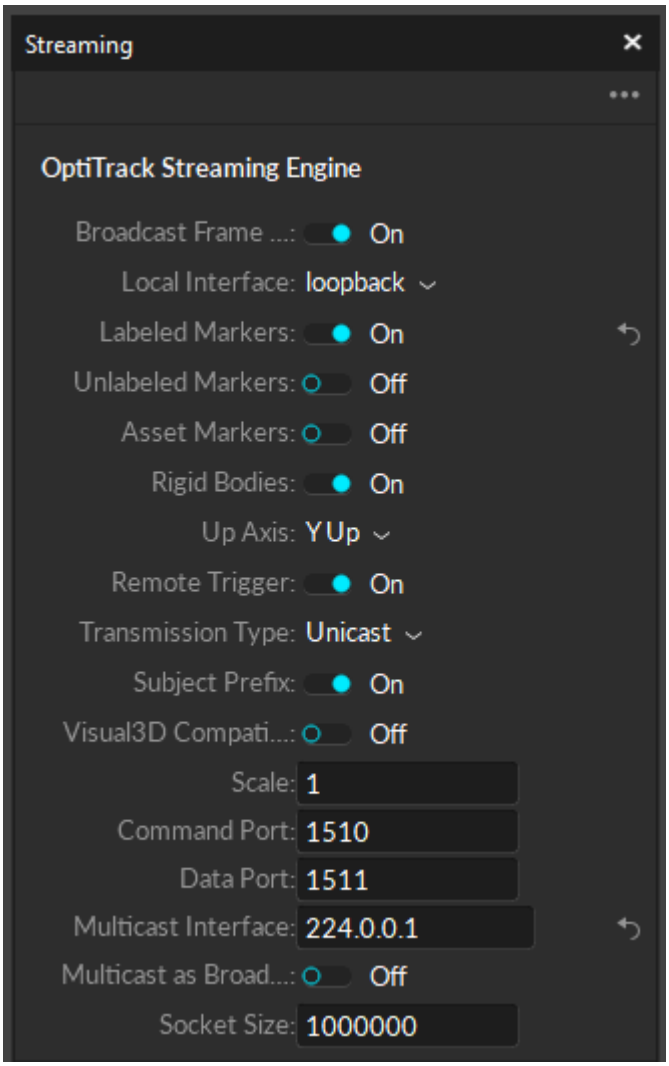

Figure 15: Optitrack Streaming Engine settings

Load cell calibration

The output of a load cell is a voltage differential. The goal of the calibration is to define the relationship between the measured voltage and the force applied.

Assuming a linear relationship between the output voltage V and the applied force F:

$$F = k * V + q \tag{1}$$

The *sensitivity* k, which represents the slope of the line, has to be found through the calibration.

The q is the bias. It represents the zeroing voltage value, but needs to be calculated once the load cells are mounted in their final position inside the MAFS, so that the weight of the structure (including the load cells own weight) is accounted for. Therefore, it will be determined at a later stage.

4.1 Calibration procedure

The calibration is done by placing proof weights on a platform connected to the load cell and reading the output voltage. The mass m and the quantity of proof weights is chosen to evenly cover the whole load cell capacity range. The measuring direction of the load cell (indicated on the load cell with an arrow) has to be parallel to the gravity vector, allowing the easy conversion: $F = \text{mass} * g$. The setup configuration is summarized in Fig. 16 and the procedure has to be repeated for each load cell. The platform mass M, as long as it remains the same throughout the entire calibration procedure, does not influence the calibration results (but only the factor q) and can be ignored.

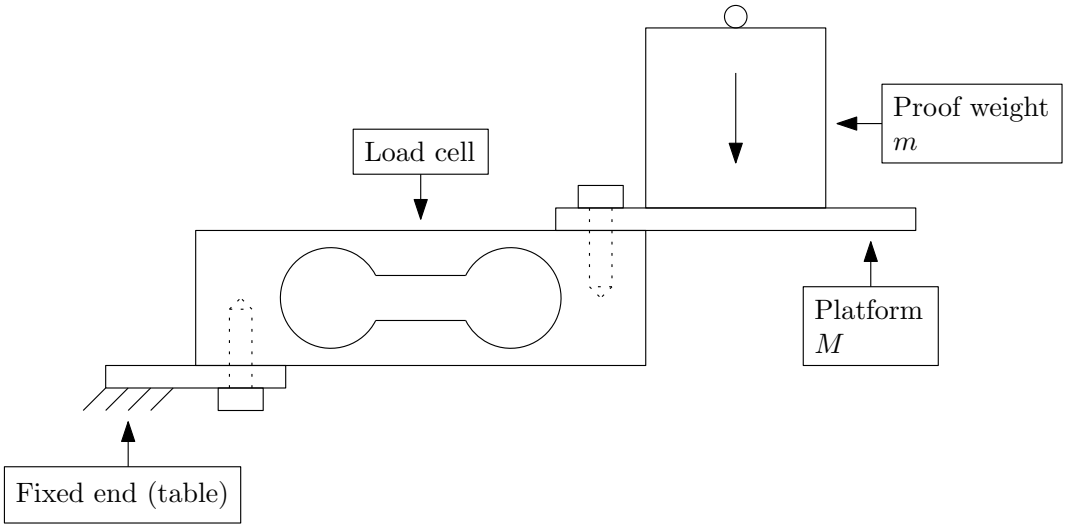

Figure 16: Load cell calibration setup

4.2 Results

Once all the data is collected, the slope k of each load cell can be calculated as the coefficient of a polynomial curve fitting using a polynomial of first degree. This is done in MATLAB with the function *polyfit*. As shown in Fig. 17a and Fig. 17b, the obtained straight lines come extremely close to all data points, confirming the validity of the linear model up to the load cell capacity limit.

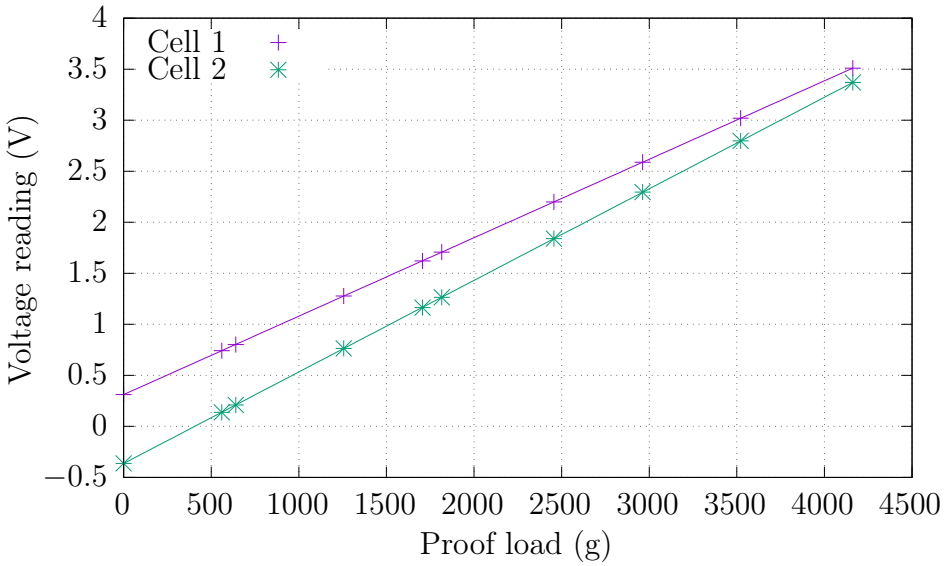

(a)

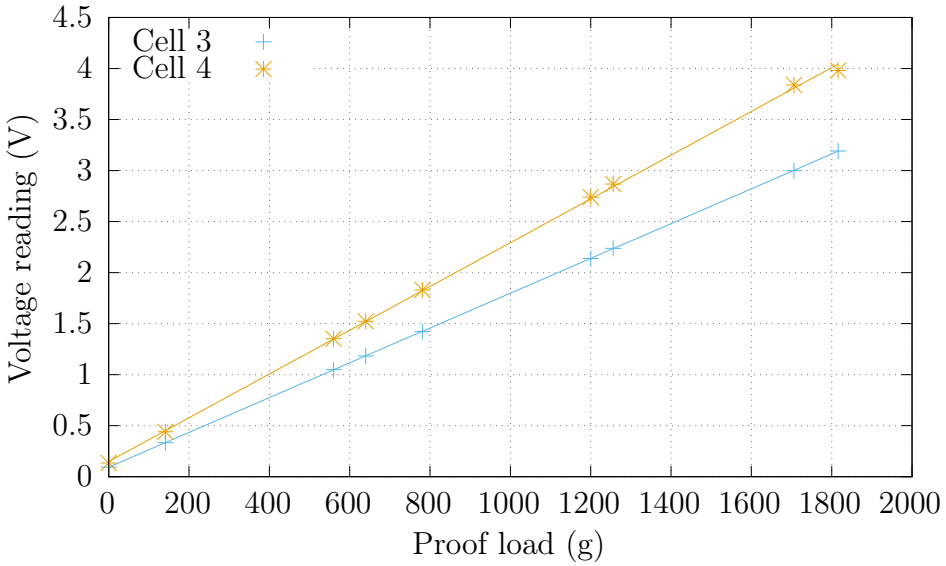

(b)

Figure 17: Calibration data. (17a) Frontal load cells (5 kg capacity limit); (17b) Lateral load cells (2 kg capacity limit).

Table 3 contains the obtained values of k. From those data it can be observed that even identical load cells (Cell 1 & 2 and Cell 3 & 4) have substantially different sensitivities. Therefore, the sensitivity is strictly representative of the tested load cell. A unique sensitivity cannot be assumed correct for other load cells, even if they are of the same model and capacity.

Table 3: Obtained Sensitivities

Load cell	Sensitivity
Cell 1	1.1146
Cell 2	1.3009
Cell 3	0.5865
Cell 4	0.4663

Static calibration

Once the four load cells are successfully calibrated, they are mounted inside the MAFS. The MAFS is capable of measuring the forces in two different directions by combining the readings of multiple cells. Because the load cells are structurally linked together, it is essential to define *how* to combine those readings and verify if the load cells sensitivities hold true once the cells are mounted. This is necessary because the desired outputs of the MAFS are the two components of the force acting on the loading plate (along the x and y axes). The equations to link those two forces to the four forces measured by the load cells have to be defined.

5.1 Calibration procedure

All the data gathered in this Chapter is obtained following a procedure similar to that one described in Chapter 4. This time, instead of a single load cell, the fully assembled MAFS is used. It is mounted to a fixed end so that one of its measuring axes is aligned with gravity. The proof weights are then placed (or hanged) on its loading plate. The frontal and lateral calibration setups are shown in Fig. 18 and 19 respectively. At the beginning of every test run, the zeroing procedure described in Appendix B is performed.

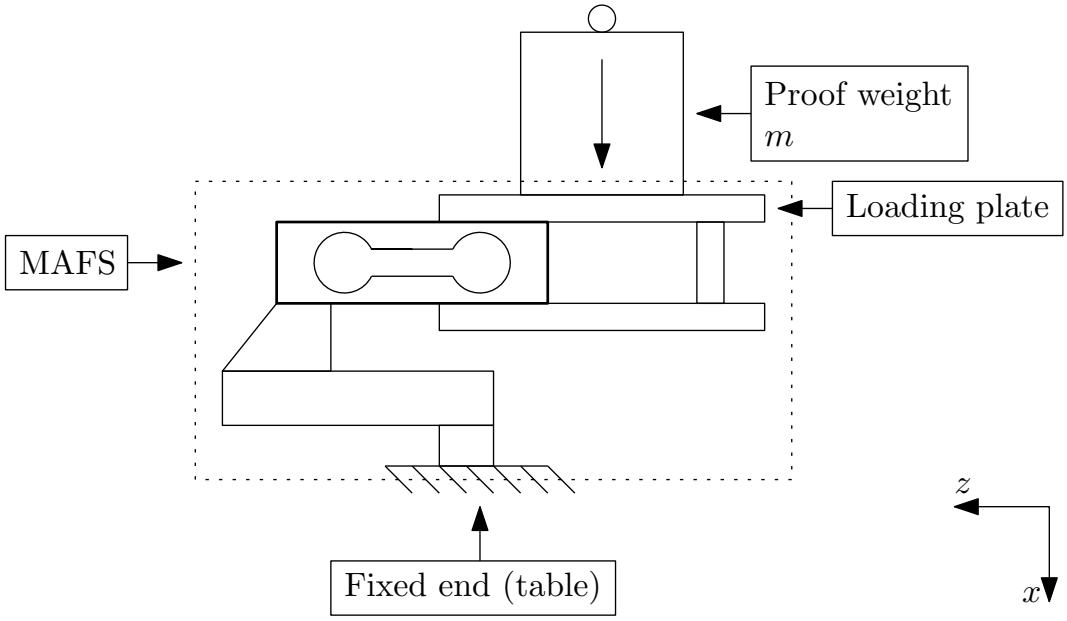

Figure 18: Frontal calibration setup, interested load cells in bold line

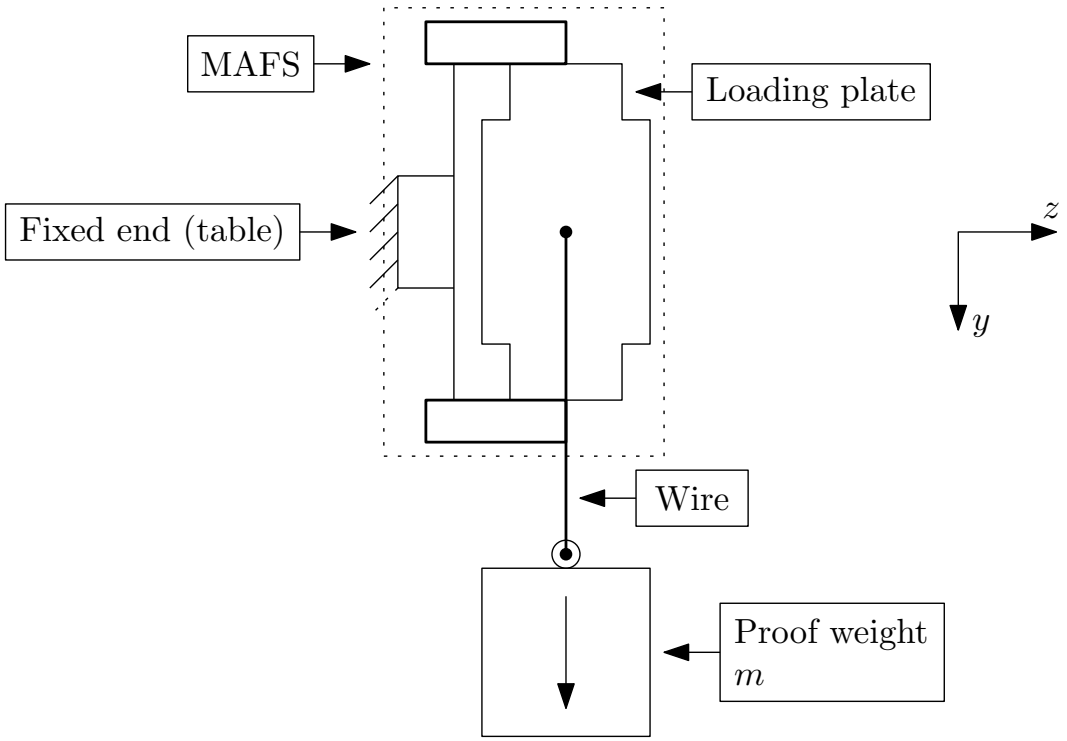

Figure 19: Lateral calibration setup, interested load cells in bold line

5.2 Frontal calibration

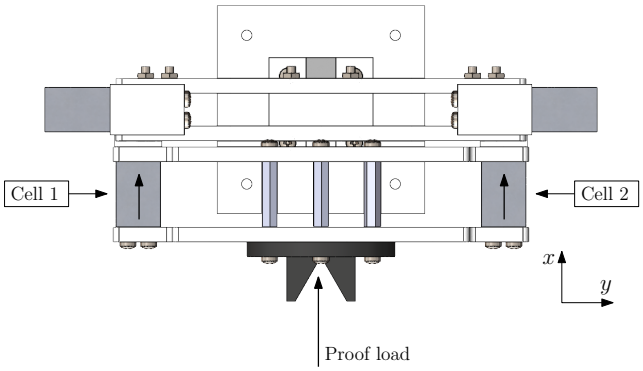

Figure 20: Visualization of the fontal load cells and proof load directions

The measuring directions of the two frontal load cells are parallel (Fig. 20). They are also in direct contact with the loading plate. This means that the model of a simply-supported beam with a concentrated point load (Fig. 21) can be used:

$$F_x = -(F_{\text{Cell 1}} + F_{\text{Cell 2}}) \tag{2}$$

The measured weight, if the MAFS frontal direction is aligned with gravity, can be found as: $W_x = F_x/g$.

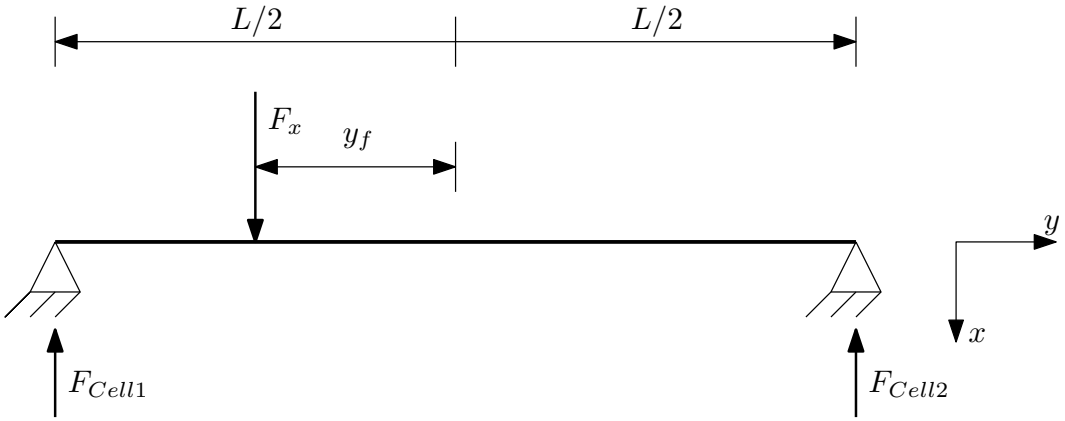

Figure 21: Simply-supported beam with a concentrated point load

The first test is performed with the proof weights positioned in the middle of the loading plate ($y_f = 0$). The data (Table 4) show the measurements of W_x are very accurate, with errors below 1.5%. This confirms that equation 2 provides correct results. Moreover, the sensitivities for Cells 1 & 2 (Table 3) remain valid and a new load cells calibration is not required.

Equation 2 should hold true even with off center loads (along the y axis), with the share of weight borne by each load cell proportional to y_f. This has been tested successfully: in Fig. 22b and 22b the total weight W_x remains equal, but the share between the two load cells varies proportionally to the y_f offset.

Eventually, a repeatability study is carried out. It is done by repeating the same measure, loading and unloading the MAFS with the same proof weight for 10 times. The results are reported in Table 5 and are satisfactory: the error remains below 1% and the measurement does not drift.

Table 4: Frontal calibration results

Proof weight [kg]	W_x [kg]	Error [%]
0.14	0.140	0.00
0.561	0.564	-0.45
1.258	1.271	-1.00
1.707	1.730	-1.33
2.268	2.271	-0.15

Table 5: Repeatability in the frontal direction with a proof weight of 1.707 kg

Test #	W_x [kg]	Error [%]
1	1.6980	0.53
2	1.7067	0.02
3	1.7007	0.37
4	1.6985	0.50
5	1.7022	0.28
6	1.7034	0.21
7	1.7034	0.21
8	1.7039	0.18
9	1.7012	0.34
10	1.7009	0.36

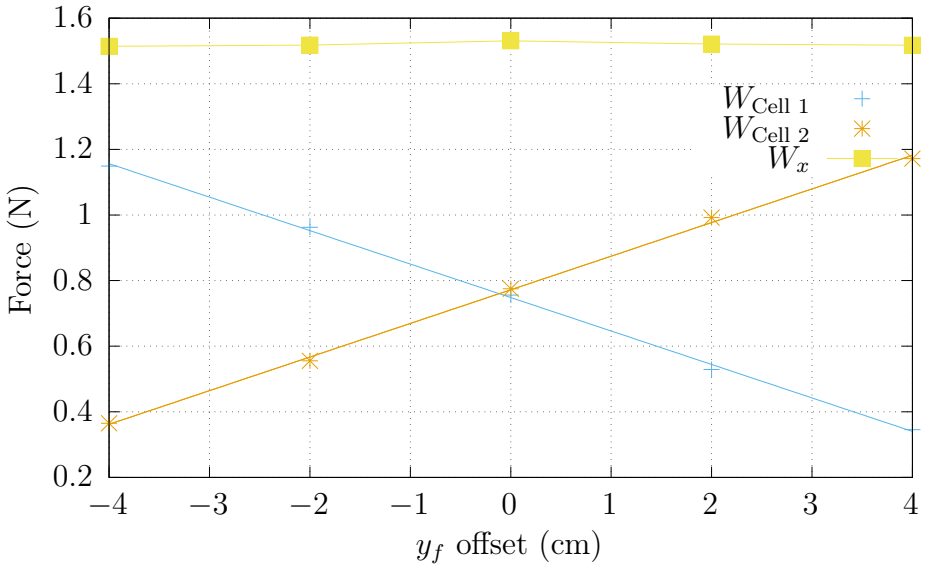

(a)

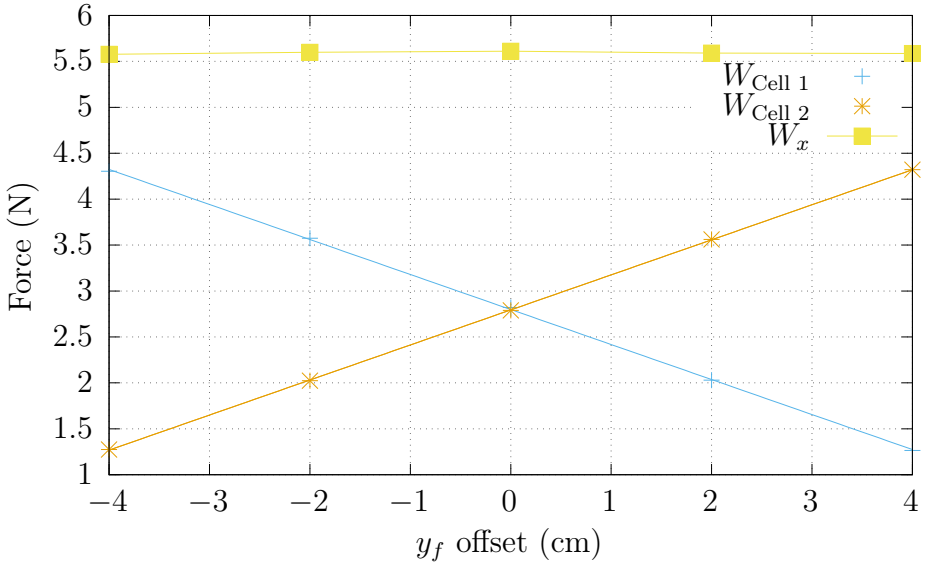

(b)

Figure 22: Off center load data. (22a) Proof load of 0.140 kg; (22b) Proof load of 0.560 kg.

5.3 Lateral calibration

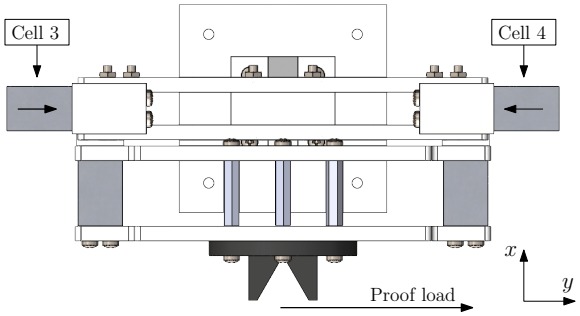

Figure 23: Visualization of the lateral load cells and proof load directions

The structural configuration of the lateral load cells (Cells 3 & 4) is different, as pictured in Fig. 23. Because they are not in direct contact with the loading plate, the structural constraints of such configuration are hard to be defined. Nevertheless, the dynamics of the lateral load cells is assumed sufficiently similar to the frontal ones. Validating this assumption is the purpose of the following tests. The total force acting in the lateral direction is calculated using an equation that mimics equation 2:

$$F_y = F_{\text{Cell 3}} - F_{\text{Cell 4}} \tag{3}$$

Again, the weight is obtained with: $W_y = F_y/g$.

Another aspect that needs to be considered is that the measuring directions of the two lateral load cells are antiparallel. The linearity of a load cell is guaranteed by the manufacturer only for positive loads. Negative (antiparallel) loads might require a different calibration or might not be measurable at all. The data in Tables 6 and 7 confirms that on both positive ($+y$) and negative ($-y$) directions the MAFS measures the load accurately, with a maximum error of 3.41% up to the load cell capacity limit. With a proof weight of 2.266 kg, which slightly exceeds the 2 kg limit, the error grows, reaching 9.6%. This

means that the capacity is not increased by the presence of two load cells; the capacity of the single load cell also represents the capacity limit of the MAFS.

Table 6: Lateral ($+y$) calibration results

Proof weight [kg]	W_x [kg]	Error [%]
0.14	0.0702	-1.93%
0.56	0.2845	-2.48%
1.258	0.6296	-3.41%
1.706	0.8123	-3.07%
1.846	0.8878	-1.24%
2.266	1.0832	7.70%

Table 7: Lateral ($-y$) calibration results

Proof weight [kg]	W_x [kg]	Error [%]
0.14	0.1388	1.50%
0.56	0.5726	-2.29%
1.258	1.2418	3.35%
1.706	1.7078	3.19%
1.846	1.869	2.49%
2.266	2.265	9.63%

The results of the repeatability test, reported in Table 8, show a peculiar behavior: whilst the error on the total load W_y is small ($< 4.5\%$) and without drift, the load repartition between the two cells (called *share*) varies greatly. There is up to a 30% variation of share, in a seemingly unpredictable pattern. This is possibly due to microscopic movements that modify the structural constraints, resulting in one cell being solicited more than the other. Because of this phenomenon, the single load cell measurement is not meaningful if not complemented with the measure of the other load cell and a relationship between the loading position and the load share cannot be established.

Table 8: Repeatability in the lateral direction ($+y$) with a proof weight of 1.707 kg

Test #	W_y [kg]	Error [%]	Share Cell 3 [%]	Share Cell 4 [%]
1	0.1454	3.86	41	59
2	0.1438	2.71	47	53
3	0.1457	4.07	42	58
4	0.1457	4.07	43	57
5	0.1458	4.14	43	57
6	0.146	4.29	44	56
7	0.1449	3.50	62	38
8	0.1453	3.79	63	37
9	0.1446	3.29	68	32
10	0.1445	3.21	60	40

Dynamic calibration

The dynamic calibration is arguably the most critical part of the MAFS calibration. If successful, the MAFS will be deemed capable of measuring docking loads.

The dynamic calibration consists in the testing of a known impact dynamics, allowing a direct comparison between the theoretical model and the values recorded by the MAFS.

Dynamic tests are substantially different from static tests and new aspects of the MAFS design and performances are involved:

- Unlike static measurements, the dynamic measurements cannot be time averaged. Sensors noise may affect the accuracy of the MAFS.
- Peak loads are greater, which may saturate the load cells or damage the structure itself.
- The addition of a motion capture system (and its synchronization with the load cell readings) may affect the MATLAB data acquisition script performances.
- Sampling frequency becomes essential. It is necessary to guarantee that it is high enough to capture the peak of the impact loads.

6.1 Drop weight and pulley setup

There are many ways to test the dynamic performances of a sensor. Because the MAFS is designed to measure impact loads, it made sense to test an impact dynamics during calibration.

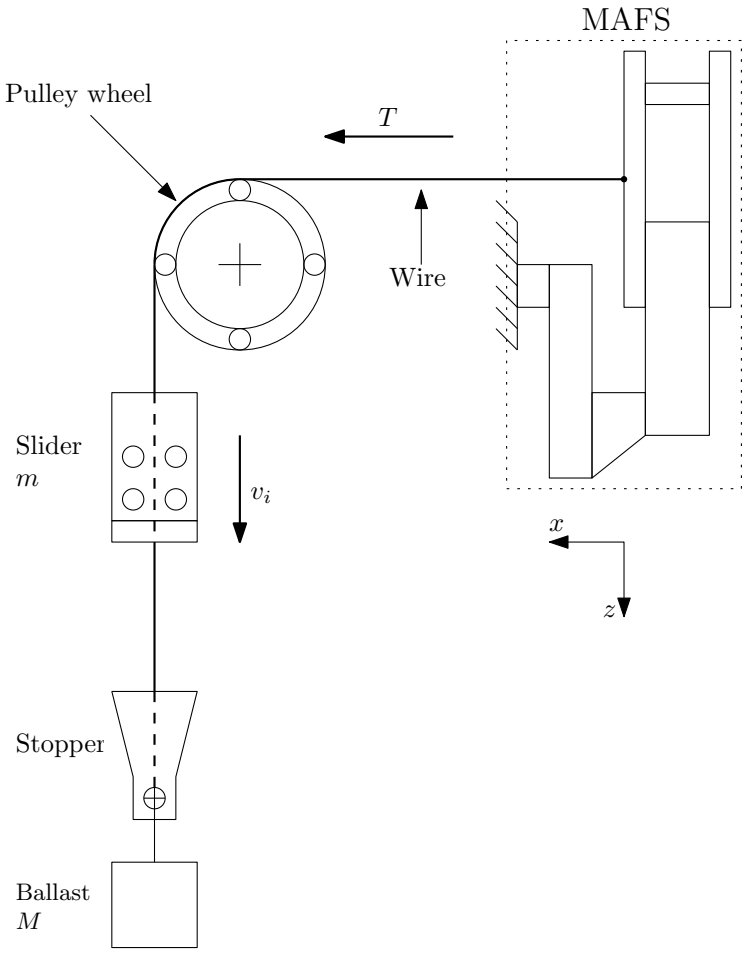

Figure 24: Drop weight and pulley setup scheme, lateral view

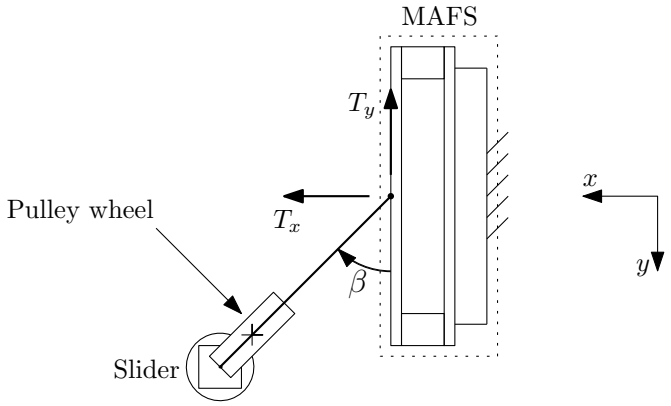

Figure 25: Drop weight and pulley setup scheme, top view

The chosen setup (Fig. 24) is a drop weight and pulley system. A weight (slider) is dropped from a fixed height. Its fall is guided by a wire. The slider will then collide with a stopper, tied at the end of the wire. On its other end, the wire is tied to the MAFS. Thanks to a pulley wheel (with ball bearing), the wire is bent 90°, allowing the MAFS to be mounted in its vertical position. A ballast is attached to the stopper in order to pretension the wire. Pretensioning the wire is critical to obtain a consistent and repeatable impact (and consequent bounce) between the slider and the stopper.

This kind of system has been chosen because:

- The impact angle can be modified by moving the pulley wheel along the y axis (see Fig. 25).
- The impact energy can be modified by changing the length of the wire.
- It allows the MAFS to be mounted in its nominal vertical position.
- It allows good repeatability.

The slider (Fig. 26) is 3D printed and has a matrix of holes used to mount the motion capture reflective markers. Because the markers cannot be too close to each other, four standoffs are used. The markers also need to be placed in a non symmetrical shape. For this reason in one of the four standoffs, the marker is replaced by two nuts of comparable weight. This is done to preserve the balance of the slider by keeping the centre of mass aligned with the central axis. The slider, including the standoffs with the reflective markers, weighs 44.1 g.

(a) Slider drawing **(b)** 3D printed model

Figure 26: Slider design

The stopper (Fig. 27) is also 3D printed. Its horizontal hole allocates a bolt used to attach the wire and the ballast. The mass of the ballast is 560 g.

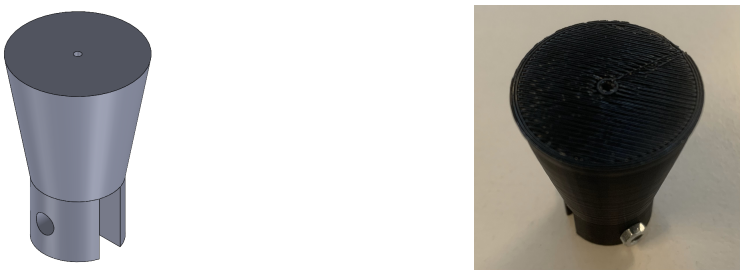

(a) CAD drawing **(b)** 3D printed model

Figure 27: Stopper design

6.2 Theoretical model

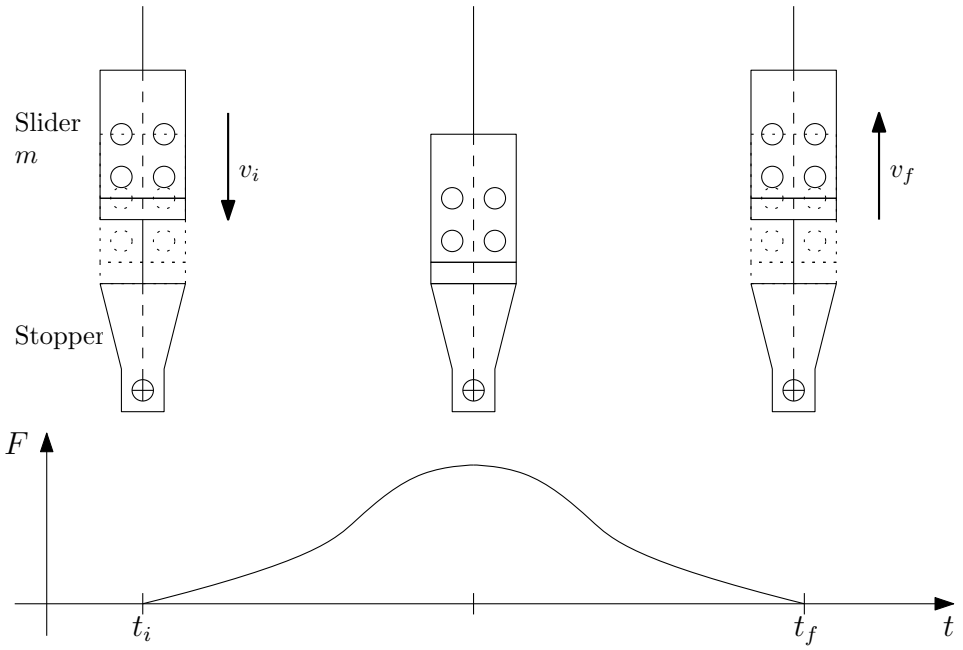

Figure 28: Impact schematization, force curve supposed symmetrical for simplicity

The physics of the slider impacting on the stopper, schematized in Fig. 28, needs to be studied. During the impact, there will be a variation in the momentum of the slider. That variation is due to the force exchanged with the

stopper. That force is zero before the contact, then it grows up to a certain point and then has to go back to be zero when the contact ends. The area of the graph represents the impulse. The impulse is defined [7] as

$$\vec{I} \equiv \int_{t_i}^{t_f} \sum \vec{F} dt \tag{4}$$

where t_i and t_f represent the time interval of the impact $\Delta t = t_f - t_i$. $\sum \vec{F}$ is the sum of the external forces.

The impulse-momentum theorem [7]

$$\vec{I} = \Delta \vec{p} \tag{5}$$

defines the fundamental relationship between the dynamics and the kinematics of the slider. During the impact, the variation of momentum of the slider is

$$\Delta p = m(v_i - v_f) \tag{6}$$

where v_i is the speed at the beginning of the contact and v_f the speed at the end of the contact. The velocity v_f can be zero if the slider actually stops, or negative if the slider bounces back. The vectorial notation is dropped as a 1D scenario is assumed, in which the velocities and forces are parallel to the wire. The impulse-momentum equation can be rewritten accordingly:

$$m(v_i - v_f) = \int_{t_i}^{t_f} \sum F dt \tag{7}$$

The sum $\sum F$ includes all the external forces acting on the slider. The gravitational force can be ignored as it remains constant during the integration interval. The setup was designed to have low sliding friction and, given the short integration interval, it should have a small impact. In conclusion, it is possible to approximate $\sum F$ as the force exchanged between the slider and the stopper $F_i(t)$. Eventually, equation 7 becomes:

$$m(v_i - v_f) = \int_{t_i}^{t_f} \sum F_i(t) dt \tag{8}$$

The force F_i exchanged during the impact is seen by the MAFS as a difference in wire tension ΔT.

6.3 Implementation

Each term of equation (8) needs to be defined and correctly measured in the laboratory environment. An explanation of how these terms are obtained follows.

Mass. The mass m is the mass of the moving object, hence the slider. Its weight is constant and is measured with a high precision scale.

Velocities. The motion capture provides accurate measurement of the position of the slider. The position of the slider in the z axis corresponds to the distance traveled when dropped.

The velocity can be obtained with the numerical derivative:

$$v_{z(i)} = \frac{P_{z(i)} - P_{z(i+1)}}{t_{(i)} - t_{(i+1)}} \tag{9}$$

where i is the motion capture frame number, $P_{z(i)}$ is the measured position in the i-th frame and $t_{(i)}$ is the timestamp of the i-th frame. An example of the obtained velocity curve (from the position curve in Fig. 29) is shown in Fig. 30. The velocity v_i is easily found as the maximum $v_{y(i)}$. Since the velocity v_f is reached in a small Δt, the sampling rate may not be high enough to capture the peak. A different approach is preferred: v_f is derived from the energy balance with equation 10, considering that the maximum height reached after the bounce h_b can be found from the positional data.

$$v_f = \sqrt{2gh_b} \tag{10}$$

Force integral. During the dynamic calibration the MAFS is zeroed with the stopper and ballast already attached. In this way, the loads measured by the MAFS directly represent the variation in wire tension. The force $F_i(t)$ in equation 8 is the vectorial sum of the frontal tension T_x and lateral tension T_y.

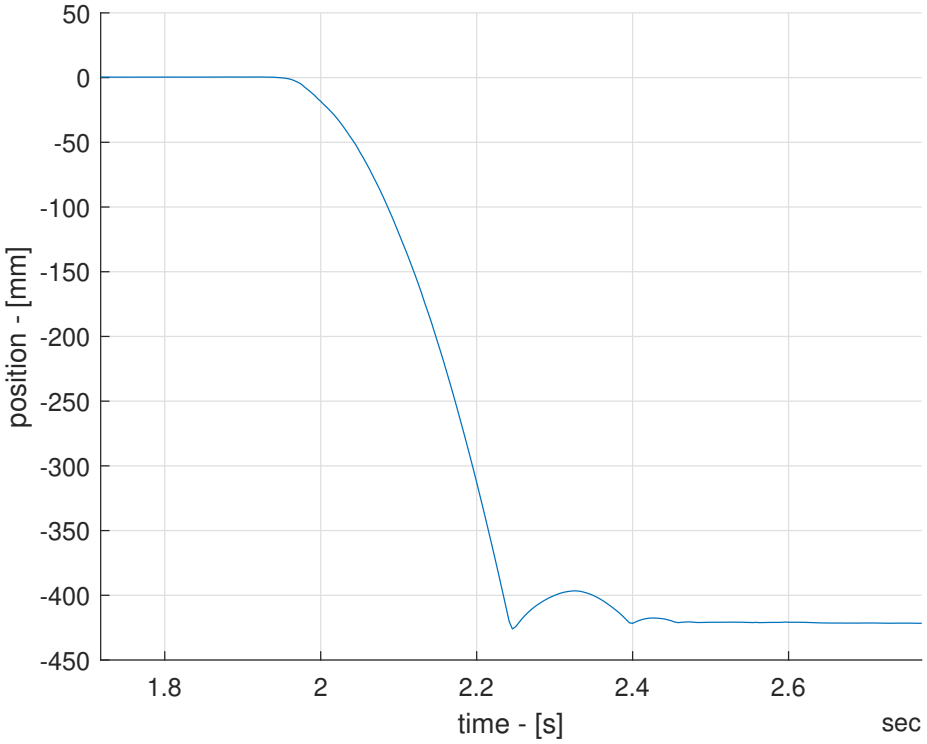

Figure 29: Motion capture measurement of the position P_z

Hence, the integral of equation 8 becomes:

$$\int_{t_i}^{t_f} F dt = \int_{t_i}^{t_f} (T_x \cos\beta + T_y \sin\beta) dt \tag{11}$$

The angle β, as shown in Fig. 25, is the angle between the normal to the loading plate and the wire. It can be physically measured, or derived from a static measure of the ballast weight as:

$$\beta = \arctan \frac{T_y}{T_x} \tag{12}$$

It has been verified during testing that the angle obtained with equation (12) differs less than $\pm 1°$ from the one measured with a protractor. Therefore, equation (12) is used during the postprocessing of the following tests.

The integration interval, defined by t_i and t_f, has some caveats that need to be addressed. The response time in the frontal and lateral direction may

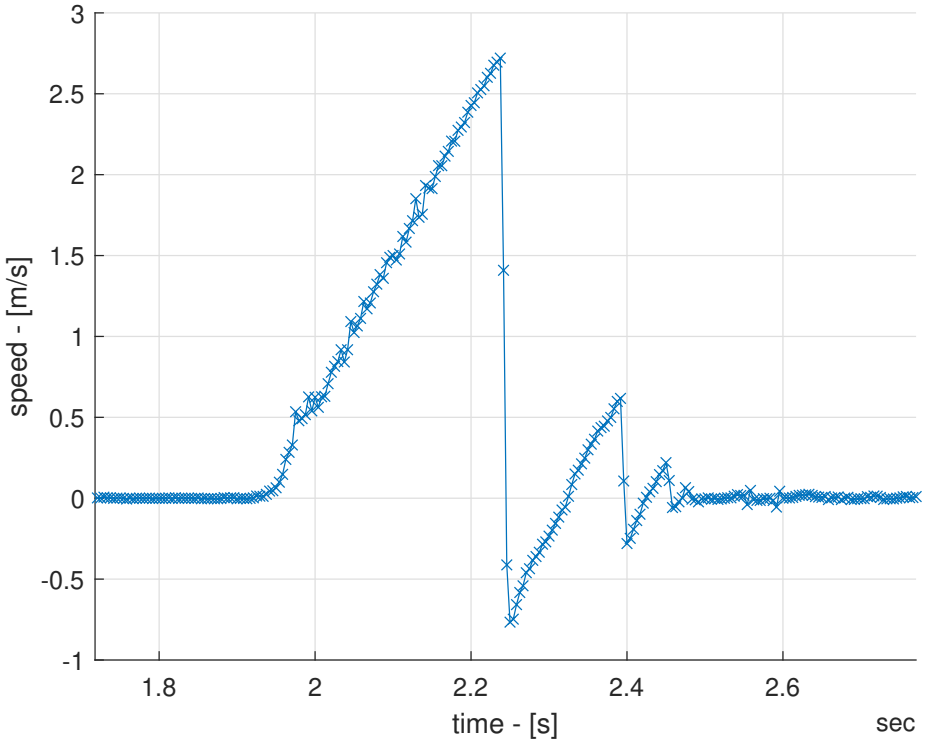

Figure 30: Obtained v_z curve

be different. This happens because the stiffness of the structure (including the load cells) changes between the two loading directions. In Fig. 31 this difference for a 45° impact is shown: the lateral load cells register a faster and higher force, whilst the frontal cells present a lower peak with a longer duration. In order to tackle this issue two different integration intervals are defined:

$$\int_{t_i}^{t_f} F dt = \int_{t_{ix}}^{t_{fx}} T_x \cos\beta dt + \int_{t_{iy}}^{t_{fy}} T_y \sin\beta dt \tag{13}$$

This approach will be justified in the following Section.

The integration is done by the MATLAB function *cumtrapz*, that computes an approximate cumulative integral via the trapezoidal method. This function outputs the integral value, given the tensions vector and the time vector [4].

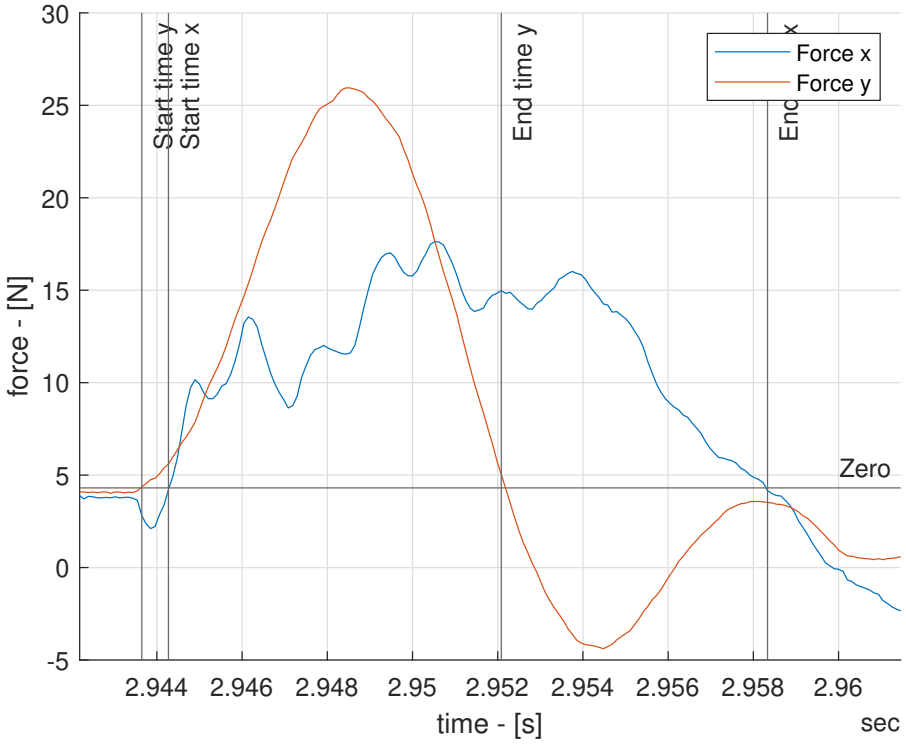

Figure 31: Loads measured in a 45° test run.

6.4 Results

The impulse I depends on the loads measured by the MAFS; by comparing the value of I with the expected variation in momentum Δp, the MAFS accuracy can be evaluated. One of the purposes of this Section is to determine the error $e = \mid I - p \mid$ and the relative error $e_r = \mid (I - p)/I \mid$ at different impact angles β. It is important to note that the momentum does not remain constant between test runs, for two main reasons:

1. The height of the bounce is variable, it is not possible to assume it as a constant, hence the need to determine it with the motion capture.

2. The slider is released by hand. Human error in height or initial velocity influences the results.

6.4.1 Frontal impact

The results of the frontal test ($\beta = 90°$) are encouraging. The relative remains below 5%, which is sufficient considering the complexity of the test.

Table 9: Frontal drop test results

Test #	Momentum [kgms^{-1}]	Impulse [Ns]	Error [Ns]	Error [%]
1	0.1508	0.1522	0.0014	0.93
2	0.1544	0.1542	0.0001	0.08
3	0.1576	0.1550	0.0026	1.66
4	0.1566	0.1549	0.0016	1.06
5	0.1576	0.1551	0.0024	1.57
6	0.1596	0.1539	0.0057	3.72
7	0.1606	0.1535	0.0071	4.63
8	0.1610	0.1591	0.0019	1.18
9	0.1601	0.1543	0.0058	3.73
10	0.1610	0.1582	0.0028	1.77

6.4.2 Lateral impact

The lateral test ($\beta = 0°$) results are acceptable, but show slightly bigger errors than the frontal test. The relative error reaches 7%.

Table 10: Lateral drop test results

Test #	Momentum [kgms^{-1}]	Impulse [Ns]	Error [Ns]	Error [%]
1	0.0934	0.0967	0.0032	3.34
2	0.0934	0.0991	0.0057	5.79
3	0.0945	0.1012	0.0067	6.66
4	0.0941	0.0967	0.0026	2.72
5	0.0940	0.0968	0.0028	2.92
6	0.0947	0.0988	0.0041	4.15
7	0.0942	0.0977	0.0034	3.53
8	0.0938	0.0964	0.0026	2.71
9	0.0943	0.0978	0.0035	3.57
10	0.0934	0.0955	0.0021	2.23

6.4.3 Angled impacts

The angled impact is the most extensive test as it embroils all the capabilities of the MAFS studied so far. Two tests are performed with the pulley positioned at 45° and 60°.

The usage of two different time intervals, one for the frontal load cells and one for the lateral load cells, described in Section 6.3, can not be verified by the previous tests. It requires both wire tension components T_x and T_y to be non-zero and this can only be true for angled impacts. Hence, the following results will be used to validate equation 13.

The test at $\beta = 45°$ (Table 11) provided results in line with the previous tests, with the relative error never exceeding 7.2%.

Table 11: Angled drop test results, $\beta = 45°$

Test #	Momentum [kgms^{-1}]	Impulse [Ns]	Error [Ns]	Error [%]
1	0.1437	0.1489	0.0052	3.48
2	0.1523	0.1609	0.0085	5.30
3	0.1489	0.1565	0.0076	4.86
4	0.1515	0.1604	0.0089	5.54
5	0.1567	0.1631	0.0065	3.96
6	0.1606	0.1589	0.0018	1.11
7	0.1529	0.1647	0.0118	7.15
8	0.1514	0.1582	0.0069	4.34
9	0.1553	0.1658	0.0106	6.37
10	0.1564	0.1615	0.0051	3.16

For the "final" test, at $\beta = 60°$, a larger sample size has been preferred, with a total of 30 drops. The average results are reported in Table 12 and provide the final confirmation that the MAFS is sufficiently accurate and consistent.

Given the positive results in the angled tests, the usage of two different integration intervals (described in Section 6.3) is considered valid.

Table 12: Angled drop test results, $\beta = 60°$

Error	Mean Value	STD
Absolute [Ns]	0.0047	0.0018
Relative [%]	2.8	1.0674

6.4.4 Frequency responses

Fig. 32 shows the frequency response of a frontal impact and the peak is at about 50 Hz. On the other hand, Fig. 33 shows the frequency response of a lateral impact and the peak is at about 115 Hz. This means that the MAFS stiffness in the lateral direction is greater. This is coherent with the lateral response being faster and steeper thant the frontal response (as previously shown in Fig. 31).

The values of peak response frequency in both directions should be greater

than the first normal mode of the docking systems that the MAFS is supposed to test. As an example, a plastic docking system tested by [6] has a natural frequency of 15 Hz. The MAFS peak response frequencies are higher, but especially in the frontal direction the MAFS peak response of 50 Hz may be too close to the one of the docking system. In order to move the MAFS response frequency to the right, stiffer materials should be used for the joints and the plates.

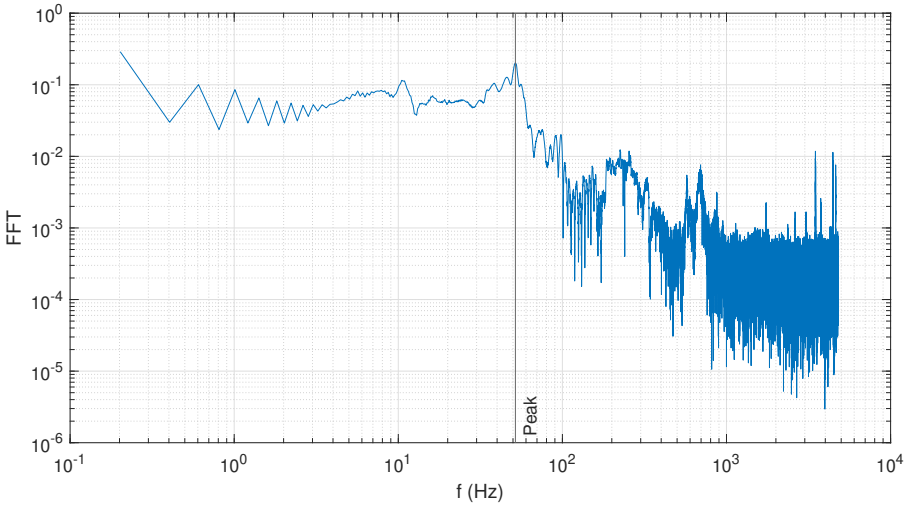

Figure 32: Obtained frequency response, frontal impact

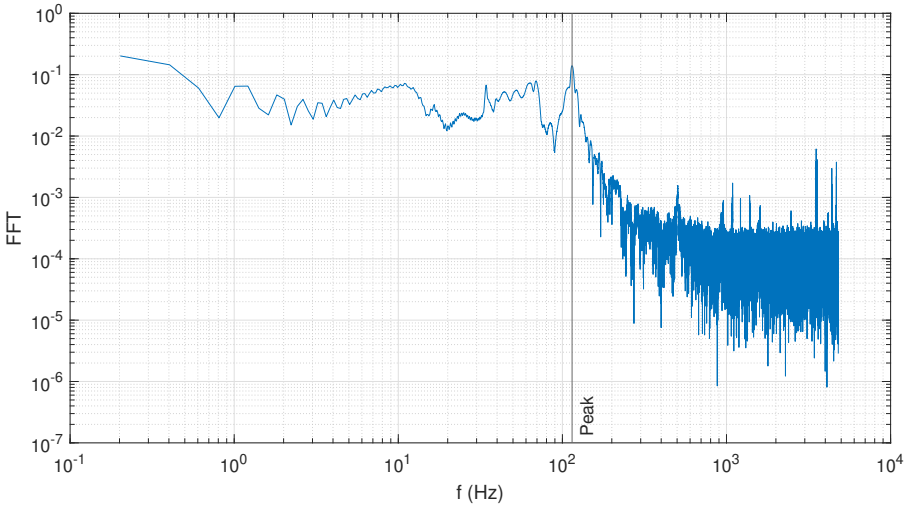

Figure 33: Obtained frequency response, lateral impact

In an angled impact (Fig. 34) the behavior resembles those obtained earlier, again with a higher peak frequency registered by the lateral load cells.

What is interesting is that, when plotting the component of the force parallel to the wire, the two responses perfectly overlap up to 15 Hz. This is possibly because the MAFS acts as a low pass filter. Being a low pass filter, the MAFS does not influence the response of the system up to the cut frequency. Because the MAFS has different stiffness in the two directions, the cut frequency and the slope of the filter may not be the same. This results in different responses between the two directions moving to the right after 15 Hz.

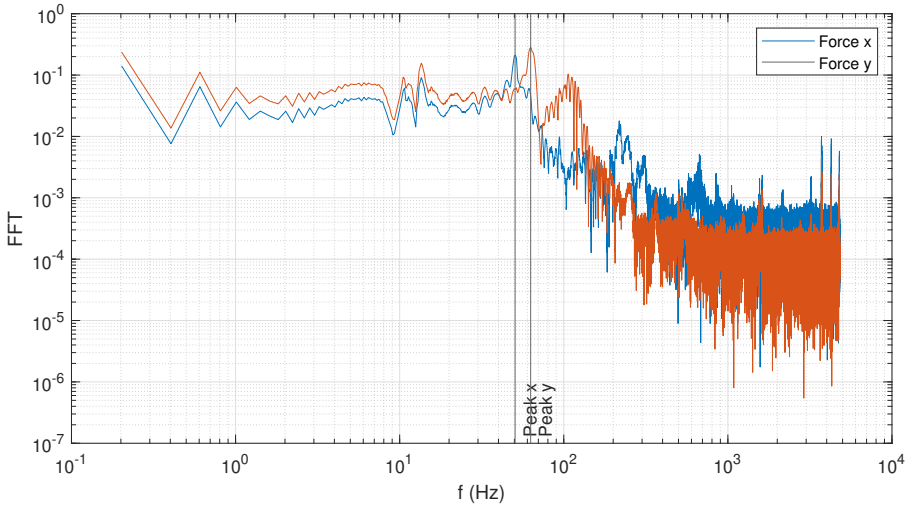

Figure 34: Obtained frequency response, angled impact ($\beta = 60°$)

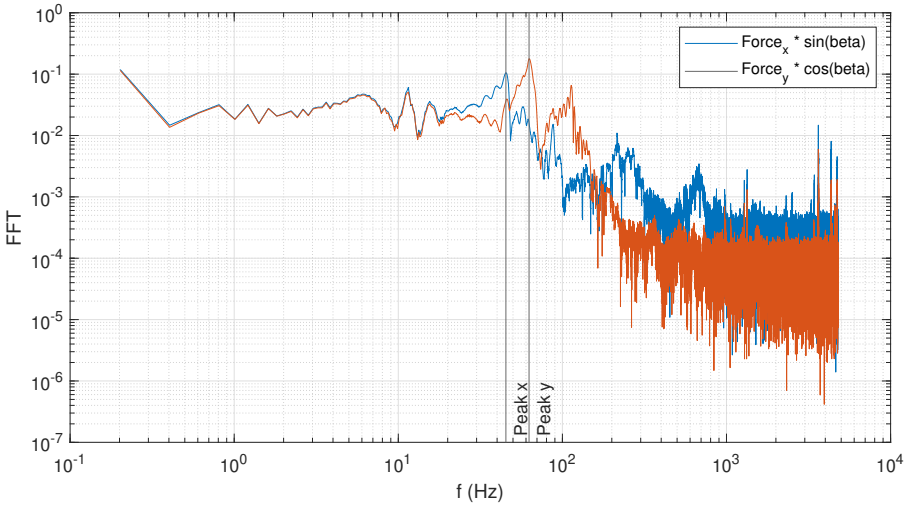

Figure 35: Obtained frequency response, angled impact ($\beta = 60°$), components parallel to T

MAFS employment

With the MAFS successfully calibrated it is possible to integrate it in the laboratory docking testing facility and proceed to employ it in a preliminary docking test.

7.1 Docking setup

The laboratory facility consists in a low-friction table and a motion capture system (Fig. 36). The low-friction table is a very rigid table covered by a flat glass surface. The satellite mockup can float on top of the table thanks to three gas cushions (Fig. 37). The pressurized gas needed by the cushions is stored in a gas tank mounted on the satellite. The table also needs to be levelled with an high-precision level. Otherwise, due to the low friction, the slope would make the satellite drift.

The motion capture system is composed of four cameras, mounted on the ceiling of the laboratory in order to have the most possibly clear line of sight. They are mounted at the four corners of the room and point at the low-friction table, that is placed roughly in the middle of the room.

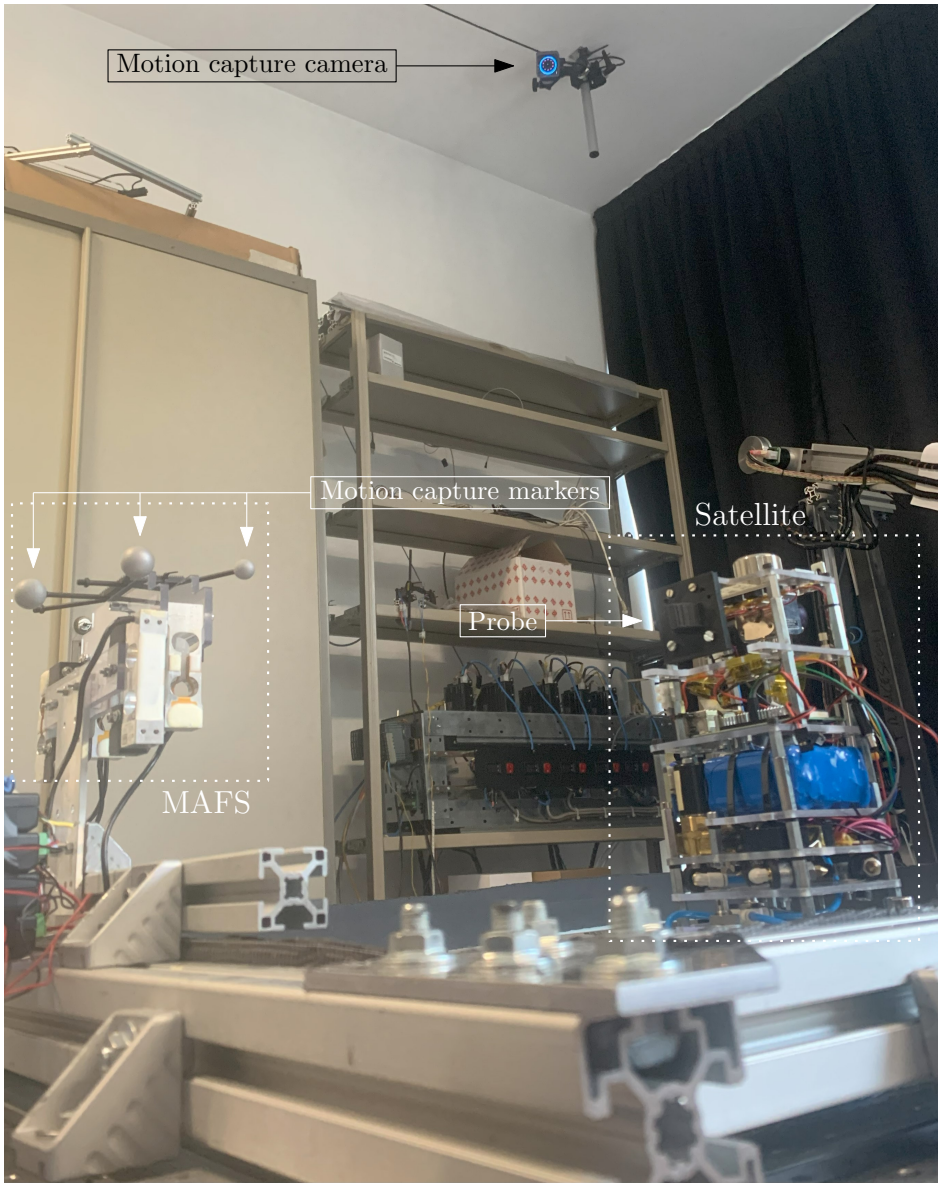

Figure 36: Laboratory facility

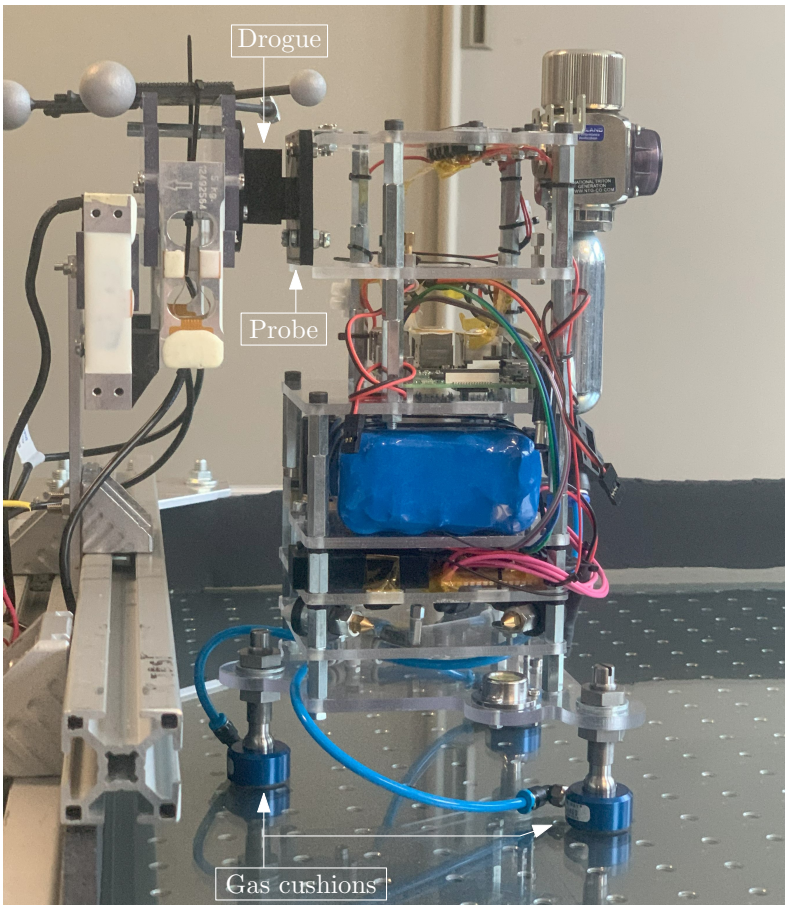

Figure 37: Satellite in contact with the MAFS

In order to perform the docking, the satellite is carefully pushed by hand towards the MAFS. The probe, mounted on the satellite, will collide with the drogue, mounted on the MAFS loading plate. Both the MAFS and the satellite are tracked by the motion capture thanks to the reflective markers. This is schematized in Fig. 38, with the reference frame zero centred on the drogue.

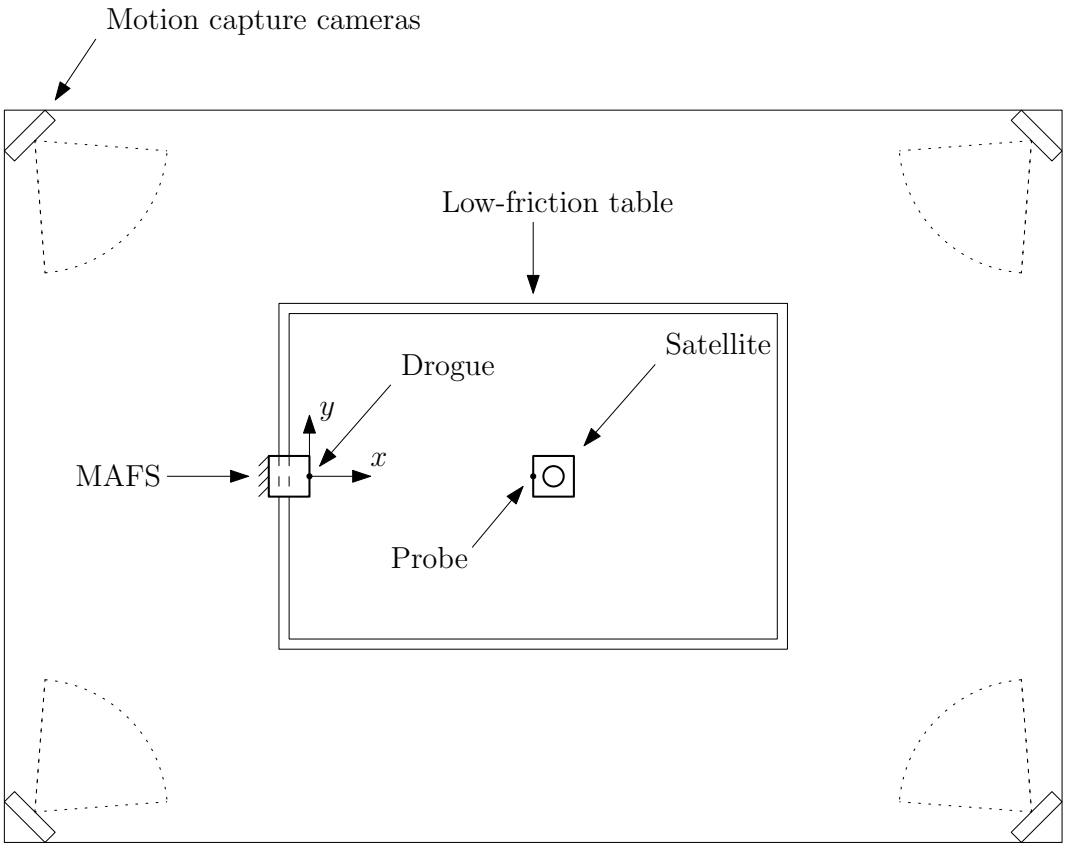

Figure 38: Scheme of the setup

A simple V-shaped geometry, detailed in Fig. 39, is chosen for the probe-drogue design. The two components are 3D printed. A smooth finish for the contacting surfaces was obtained through sanding. The main geometric constraint is that the section has to remain constant in the z direction. This is necessary to minimize the loads exchanged along the z axis, which may upset the gas cushions distance from the glass surface, increasing friction. The V-shape allows the probe to be self-centering in the y axis whilst advancing in the x direction, remaining neutral in the z direction.

Given the low friction and the lack of a retention mechanism, after the probe collides with the drogue, the satellite is expected to bounce back. This means that it will not reach a steady state after the impact.

(a) Top view **(b)** Perspective view

Figure 39: CAD model of the V-shaped probe-drogue design

7.2 Results

Two *types* of docking are conducted, defined by their visual outcomes:

a. **Impact with bounces**: the probe tip hits one of the two V-shaped walls first, resulting in a series of bounces between the two walls.

b. **Precise impact**: the probe is perfectly centred on the drogue and the are no visual bounces from one V-shaped wall to the other.

The plots in Fig. 40 confirm the visual observations. In the first impact at least four bounces are clearly shown by the peaks. The peaks in the frontal direction are all positive, whilst in the lateral direction are alternated, which justifies a bouncing motion. The frontal peak force is 4.37 N and the lateral peak force is 6.70 N. In this case, the frontal and lateral load peaks are comparable, with the lateral one actually being the greatest. The lateral peak happens on the second bounce, which is unexpected. The impact duration is about 0.02 seconds.

The second impact, as expected, presents one big peak of loads for both the frontal and lateral directions. The frontal peak force is 8.53 N and the lateral peak force is 2.67 N. It is interesting to note that even an apparently perfectly aligned docking produced a not negligible lateral load. The impact duration is longer, at about 0.6 seconds.

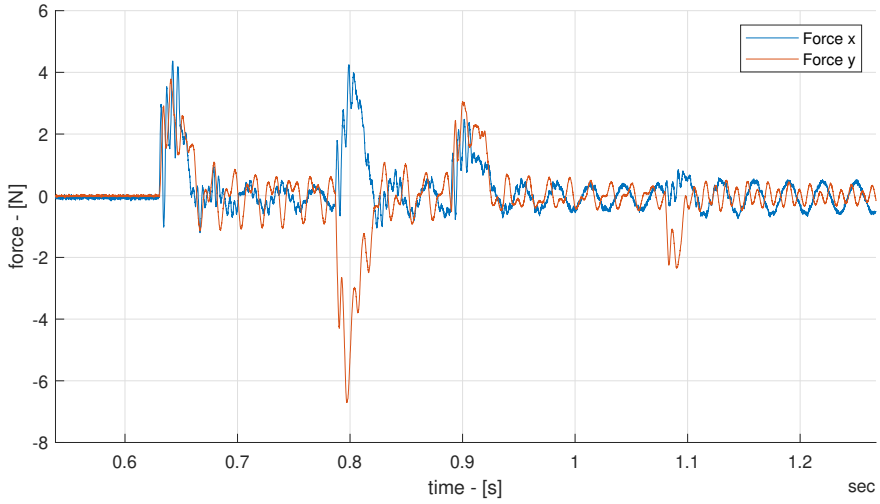

(a)

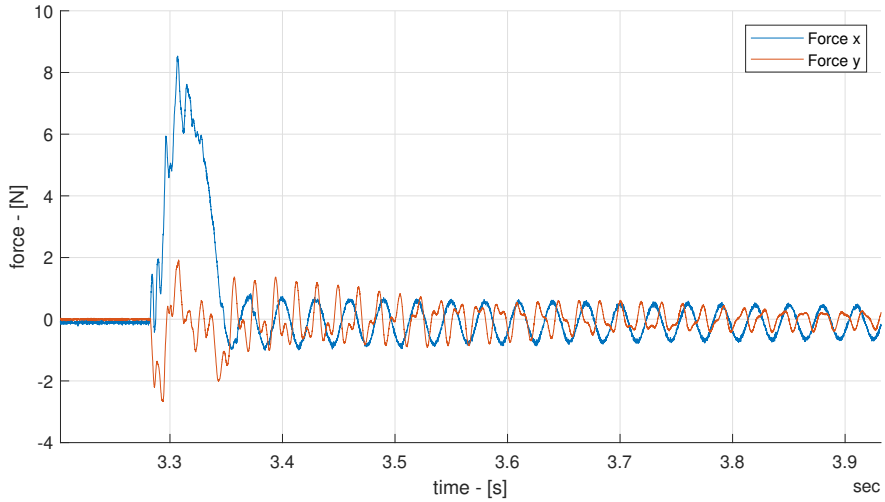

(b)

Figure 40: Docking loads plots. (40a) Impact with bounces; (40b) Precise impact.

The motion capture data in Fig. 41 provides meaningful information regarding the satellite position, keeping in mind that the zero is set with the probe perfectly docked into the drogue:

- The distance in the x direction comes close (< 1 mm) to zero, meaning that the probe reached the maximum depth. After that, the satellite bounces back and the distance keeps growing, as expected due to the lack of a retention mechanism. This is true for both impact types.
- In the y direction, the position of first contact is 2 mm away from the center of the probe for the precise impact, whilst it grows to 6 mm for the impact with bounces. This is reasonable and suggests that the bounces are caused by the increased misalignment between the probe and the drogue on first contact.
- In both impact types, the position in the z direction remains extremely close to zero. This confirms that the satellite is moving on a flat and levelled surface.

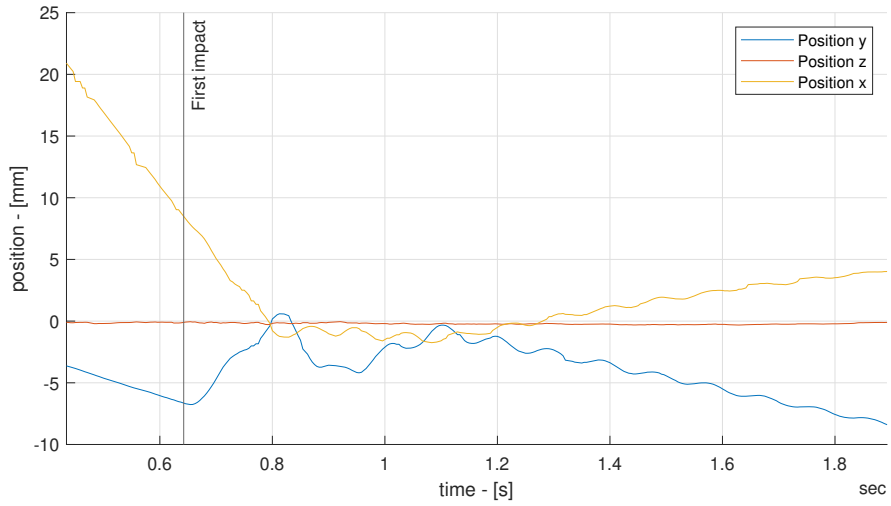

(a)

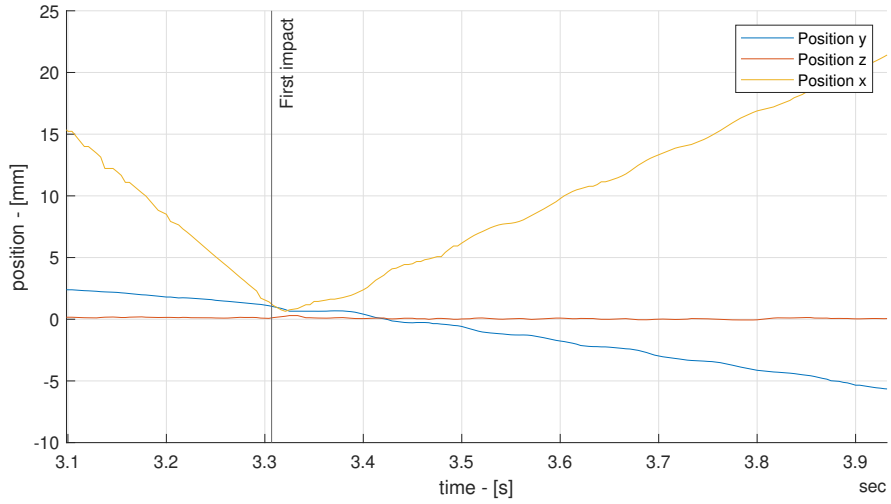

(b)

Figure 41: Docking satellite position plots. (40a) Impact with bounces; (40b) Precise impact.

The motion capture data also outputs the angle of the satellite about the z axis. It is plotted in Fig. 42 and the zero is set when the probe and the drogue are perfectly parallel. A positive slope represents a clockwise rotation, whilst a negative slow represents an anticlockwise rotation.

In the impact with bounces, the first three hits modify the rotation direction as expected (at 0.65, 0.81 and 0.91 seconds), alternating clockwise and anticlockwise rotations. The following smaller bounces do not seem to affect the rotation direction and the angle keeps growing. That is unavoidable given the lack of retention or latching mechanisms.

In the precise impact there are no changes in the rotation direction and the impact with the drogue does not affect the satellite rotation at all. The angle keeps growing, meaning that the satellite is rotating clockwise, unaffected by the impact. This confirms the absence of bounces of the probe between the two walls of the drogue: those bounces would cause the rotation to change from clockwise to anticlockwise at least once.

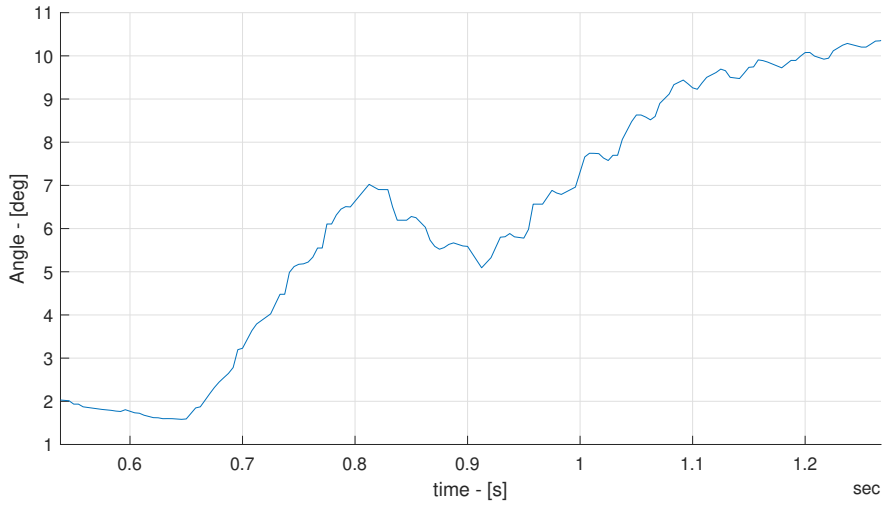

(a)

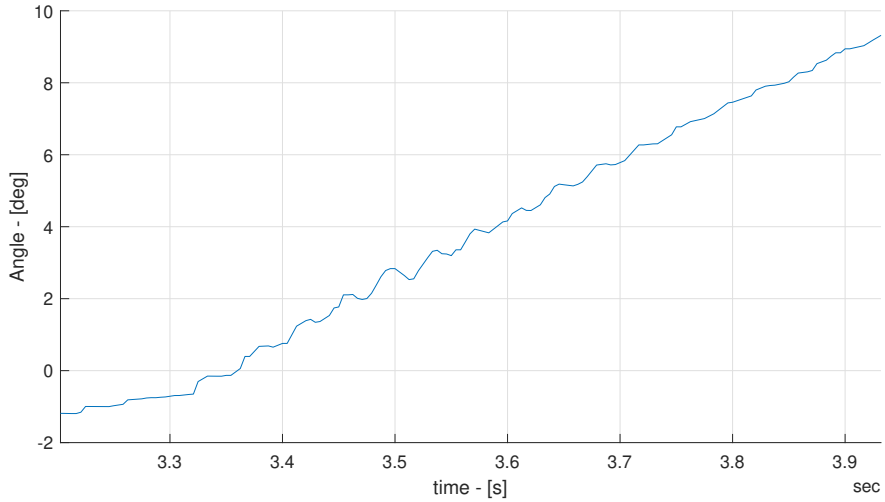

(b)

Figure 42: Docking satellite z angle plots. (40a) Impact with bounces; (40b) Precise impact.

Conclusions

The purpose of this thesis was to provide an overview on the development and testing of a multi axial force sensor for docking systems characterization.

8.1 Calibration takeaways

The static calibration confirmed that the unconventional structural constraints of the load cells do not affect their measurements: the MAFS is able to measure static loads (up to its capacity range) accurately and consistently.

The dynamic calibration results also looked promising. The dynamic setup is definitely more complex than the static one, and given the numerous variables that come into play, consistently remaining below a relative error of 8% can be considered a success.

Some concerns regarding the structural rigidity of the MAFS are yet to be addressed. Additional tests utilizing a stiffer structure and/or different load cells could help understanding which is the most effective way to increase the peak response frequency.

8.2 Future improvements

The ability to measure the torque about the z axis would give useful data for docking systems characterization. One possible way to get a torque measure is taking advantage of the two frontal load cells.

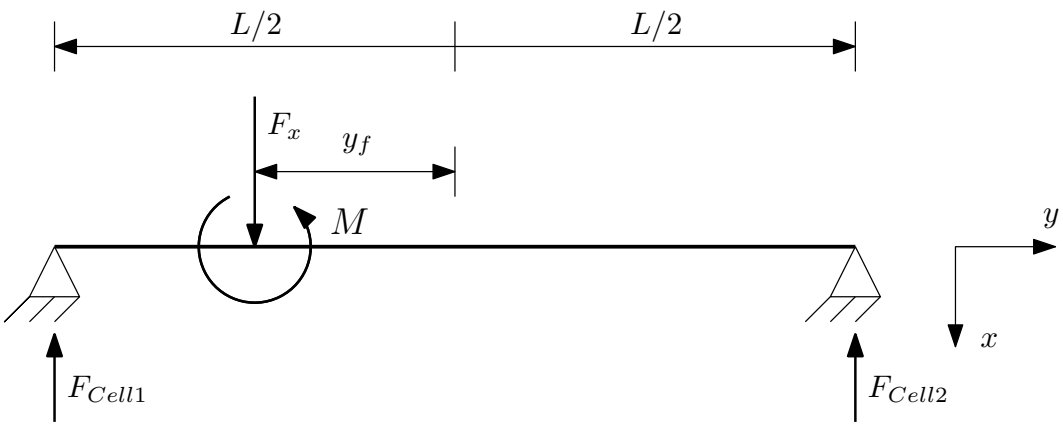

Figure 43: Simply-supported beam with a concentrated point load and moment applied

The loading plate, which is schematized in Fig. 43 as simply supported beam (discussed in Section 5.2) is subject to a load and a moment, both applied in the same position. The applied moment M can be determined with the moment equilibrium equation

$$M = F_{\text{Cell 1}}(L/2 - y_f) - F_{\text{Cell 2}}(L/2 + y_f) \tag{14}$$

where y_f is the point of contact between the probe and the drogue. This approach does not require any additional hardware and the calculation can be performed in postprocessing. Additional tests should be done to verify the validity and accuracy of the measurements. The distance y_f is hard to be determined accurately because it changes depending on the relative probe-drogue position of contact, because the probe does not hit the drogue in the same exact position every time.

In order to solve this issue and obtain more accurate readings a torque sensor can be used, for example a Futek *FSH03981* reaction torque sensor. This sensor also features a thru-hole design, that allows the MAFS cables to be run through a hole in the center of the sensor, reducing the influence of the wires rigidity on the torque measurement.

Currently, the vertical alignment (along the z axis) of the MAFS is done by modifying the mounting position. A more practical and accurate solution could be the addition of an optical stage between the fixed mounting point and the MAFS. The optical stage would allow to fine tune the height, which

is necessary to successfully test probe-drogue mechanisms with more complex geometries.

The MAFS updated with the optical stage and the torque sensor is pictured in Figures 44a and 44a.

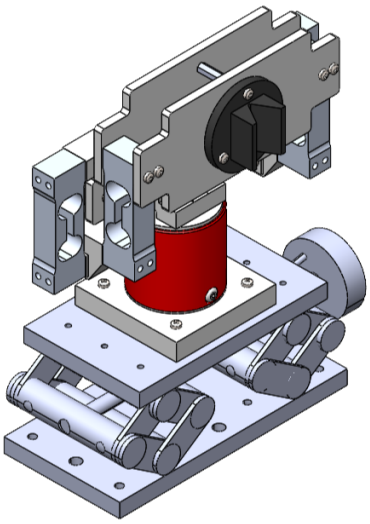

(a)

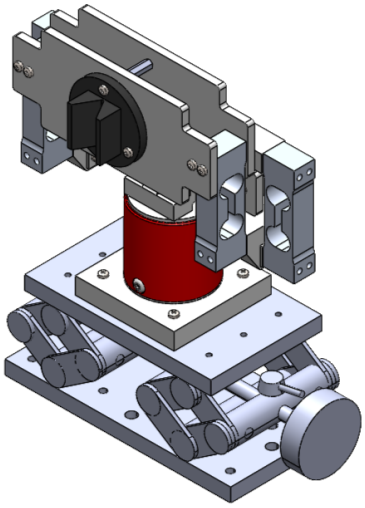

(b)

Figure 44: CAD model of the enhanced MAFS

In summary, the main improvements for the MAFS are:

- Enabling torque measuring capabilities:

  - Through the frontal load cells readings, with a properly developed postprocessing script
  - With a dedicated torque sensor
- Inclusion of an optical stage for precise height tuning
- Stiffening of the structure utilizing aluminum joints and plates

8.3 Present and future MAFS employments

When the MAFS has been employed in the docking setup, a basic probe and drogue design was utilized, but it still provided interesting insights on the impact dynamics. For example, the ability to recognize the number and the intensity of the small bounces between the two V-shaped walls is a proof of the usefulness of the MAFS for docking systems characterization.

Naturally, this is just the beginning: more studies will follow utilizing more complex docking mechanisms. For instance, measuring the loads exchanged in presence of latching or retention mechanisms could provide meaningful results.

Overall, the MAFS proved to be a good tool and it will be integrated in the laboratory setup, complementing the other capabilities of the laboratory facility used for docking studies. Even tough some improvements to its design will be needed, it is off to a good start.

Data acquisition code

The MATLAB code used to acquire the MAFS data (including the motion capture data) is summarized in Fig. 45. It is composed of a main script called *dataAcquisition.m* and an event handler called *logPosition.m* which is called each time a new motion capture frame is received.

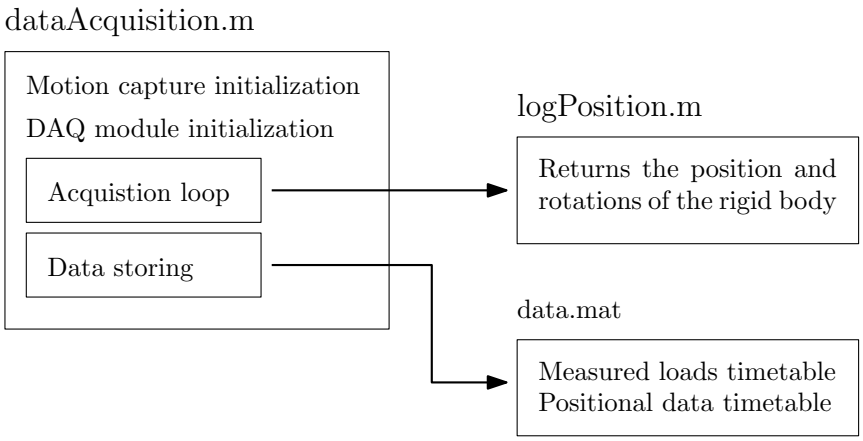

Figure 45: MATLAB code scheme

To perform a new data acquisition, the main script needs to be run. During the initialization procedures, the sensitivities and biases of the load cells are set, to allow the conversion from voltage to force. The acquisition loop duration can be modified depending on the requirements of each measurement. For static measurements, it is set at 10 seconds. At the end of the acquisition, the collected data is saved in the form of timetables in a data.mat file. It can be later loaded in MATLAB for postprocessing analyses.

A.1 DAQ module code

Algorithm A.1: DAQ module initialization (dataAcquistion.m)

```
device = daq("mcc"); % create a DataAcquisition object
ch0 = addinput(device, "Board0", "Ai0", "Voltage"); %
   add channel
ch0.Range = [-10, 10]; %set range
ch0.TerminalConfig = 'SingleEnded'; %set input mode
ch1 = addinput(device, "Board0", "Ai1", "Voltage");
ch1.Range = [-10, 10];
ch1.TerminalConfig = 'SingleEnded';
ch2 = addinput(device, "Board0", "Ai2", "Voltage");
ch2.Range = [-10, 10];
ch2.TerminalConfig = 'SingleEnded';
ch3 = addinput(device, "Board0", "Ai3", "Voltage");
ch3.Range = [-10, 10];
ch3.TerminalConfig = 'SingleEnded';
```

A.2 Motion capture code

Algorithm A.2: Motion capture initialization (dataAcquistion.m)

```
    global px1 py1 pz1
    global time1
    global rbnum
    rbnum = 1; % set rigid body ID number
    natnetclient = natnet; % create an instance of the
        natnet client class
    natnetclient.HostIP = '127.0.0.1';
    natnetclient.ClientIP = '127.0.0.1';
    natnetclient.ConnectionType = 'Unicast';
    natnetclient.connect; % connect the client to the
       server (multicast over local loopback)
    if ( natnetclient.IsConnected == 0 )
            fprintf( 'Client failed to connect\n' )
```

```
12                  return
13          end
14          natnetmodel = natnetclient.getModelDescription;
15          disp(['Rigid body tracked: ', natnetmodel.
               RigidBody(rbnum).Name]); % print rigid body
               name
16          addpath('event handlers') % point to event
               handlers folder
17          natnetclient.addlistener( 1 , 'logPosition' ); %
               add listener
```

Algorithm A.3: Event handler (logPosition.m)

```
1  function logPosition( ~ , evnt )
2          % The event callback function executes each time a
               frame of mocap data is delivered
3          global px1 py1 pz1
4          global time1
5          global rbnum
6
7          % Get the rigid body position and timestamp
8          time1(end+1) = evnt.data.fTimestamp;
9          px1(end+1) = evnt.data.RigidBodies( rbnum ).x;
10         py1(end+1) = evnt.data.RigidBodies( rbnum ).y;
11         pz1(end+1) = evnt.data.RigidBodies( rbnum ).z;
12 end
```

A.3 Acquisition loop

Algorithm A.4: Acquisition loop (dataAcquistion.m)

```
1  natnetclient.enable(1) % run and execute eventhandler
      queues until removed
2  pause(testTime) % acquisition time
3  natnetclient.disable(1) % disable mocap listener
4  mcData = array2timetable([px1' py1' pz1'], 'RowTimes',
      seconds(time1-time1(1)));
```

```
5 mcData = renamevars(mcData, ["Var1", "Var2", "Var3"], ["px
    ", "py", "pz"]); %rename timetable variables
6 mcData = sortrows(mcData); % in case timestamps are not
    sorted (events listener functions are async)
```

MAFS zeroing

The software zeroing of the MAFS consists in the determination of the appropriate bias coefficients for each load cell. Equation 1 can be conveniently modified into

$$F_i = k_i * (V_i + q_i^*) \tag{15}$$

where F_i represents the calculated force acting on the i-th load cell. The sum $V_i + q_i^*$ needs to equal zero when the MAFS is unloaded.

B.1 Zeroing procedure

The following procedure is followed each time the MAFS required to be zeroed:

1. Verify that the PSU voltage is set at 10 V and all cells are connected correctly.
2. Verify that the MAFS is unloaded, without anything touching the loading plate. All the wires and cables also need to be positioned so that they do not touch the MAFS.
3. Run the data acquisition script with an acquisition loop duration of 10 seconds.
4. Calculate the time average of the voltage outputs $\overline{V_i}$.
5. Determine the bias as: $q_i^* = -\overline{V_i}$.
6. Update the data acquisition script with the new q_i^*.

Table 13 provides an example of the bias q_i^* obtained following the aforementioned zeroing procedure.

Table 13: Sample of bias factors

Load cell	Bias
Cell 1	-0.62628
Cell 2	0.41080
Cell 3	-0.20627
Cell 4	-0.25667

The load cells used by the MAFS are really susceptible and require frequent zeroing. Even if the MAFS is left unloaded, within a couple of hours the zero drifts and requires a new zeroing.

Naturally, each time the MAFS orientation is changed a new zeroing is mandatory.

Bibliography

[1] Francesco Branz et al. "Miniature docking mechanism for CubeSats". In: *Acta Astronautica* 176 (2020), pp. 510–519. ISSN: 0094-5765. URL: https://www.sciencedirect.com/science/article/pii/S0094576520304082.

[2] *EL-R and EX-R DC Power Supply data sheet*. Issue 1. Aim and Thurlby Thandar Instruments. 2016.

[3] NaturalPoint Inc. *NatNet: Matlab Wrapper*. 2022. URL: https://docs.optitrack.com/developer-tools/natnet-sdk/natnet-matlab-wrapper.

[4] The MathWorks Inc. *Cumulative trapezoidal numerical integration*. Natick, Massachusetts, United States, 2022. URL: https://www.mathworks.com/help/matlab/ref/cumtrapz.html.

[5] *Load Cell and Weigh Module Handbook*. Rice Lake Weighing Systems. 2019.

[6] Lorenzo Olivieri and Alessandro Francesconi. "Design and test of a semiandrogynous docking mechanism for small satellites". In: *Acta Astronautica* 122 (2016), pp. 219–230. ISSN: 0094-5765. URL: https://www.sciencedirect.com/science/article/pii/S0094576516000515.

[7] R. Serway and J. Jewett. *Physics for Scientists and Engineers with Modern Physics, Chapters 1-46*. Cengage Learning, 2008. ISBN: 9780495112457. URL: https://books.google.it/books?id=eOU9AQAAIAAJ.

[8] *SY011 Versatile In-line Bridge Amplifier*. Synectic Design Ltd.

[9] *Technical Specifications Pavone Systems 1006*. PWS34320220331. Pavone Sistemi S.R.L.

[10] Jack O. Templeman, Brian B. Sheil, and Tong Sun. "Multi-axis force sensors: A state-of-the-art review". In: *Sensors and Actuators A: Physical* 304 (2020), p. 111772. ISSN: 0924-4247. URL: https://www.sciencedirect.com/science/article/pii/S0924424719308842.

[11] *USB-1408FS-Plus User's Guide*. Revision 4a. Measurement Computing Corporation. Nov. 2014.